A SEMANTIC TOUCH INTERFACE FOR FLYING CAMERA PHOTOGRAPHY

by

LAN ZIQUAN

B.Comp. (Computer Science, NUS) 2013
B.Sci. (Applied Mathematics, NUS) 2013

A THESIS SUBMITTED FOR THE DEGREE OF

DOCTOR OF PHILOSOPHY

in

COMPUTER SCIENCE

in the

DEPARTMENT OF NUS GRADUATE SCHOOL
FOR INTEGRATIVE SCIENCES AND ENGINEERING

of the

NATIONAL UNIVERSITY OF SINGAPORE

2019

Supervisor:
Professor David HSU

Examiners:
Associate Professor Marcelo Jr. H. ANG
Assistant Professor Brian Y. LIM
Associate Professor Ping TAN, Simon Fraser University

Declaration

I hereby declare that this thesis is my original work and it has been written by me in its entirety. I have duly acknowledged all the sources of information which have been used in the thesis.

This thesis has also not been submitted for any degree in any university previously.

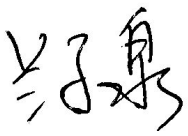

Ziquan Lan

31 Dec 2018

Acknowledgements

First and foremost, I would like to express my heartfelt gratitude to my thesis advisor David Hsu for the guidance and support. His insights in Robotics have been continuously guiding me even before my PhD study. David is also a life mentor who is always supportive during my ups and downs. I am truly grateful.

Next, I would like to thank Shengdong Zhao and Gim Hee Lee for sharing with me their insights in Human Computer Interaction and Computer Vision during the project discussions. Their suggestions across different research fields enable me to complete this interdisciplinary thesis. In addition, my special thanks goes to Wee Sun Lee for his constructive feedback during the group meetings.

I also thank Marcelo Jr. H. Ang, Brian Y. Lim and Ping Tan for providing constructive feedback to improve the quality of my thesis.

The members in our AdaComp Lab are a group of wonderful people. Mohit Shridhar is my project partner. I will always remember the experiences when we worked together towards those demo and paper deadlines. Also, I received tremendous help from my labmates, Haoyu Bai, Andras Kupcsik, Nan Ye, Zhan Wei Lim, Kegui Wu, Shaojun Cai, Min Chen, Juekun Li, Neha Garg, Yuanfu Luo, Wei Gao, Peter Karkus, Xiao Ma, Panpan Cai, Devesh Yamparala, etc.

In addition, I have been also working among people from other research labs as well. Experiences and ideas from different perspectives inspired me along the way. I would like to thank the seniors, Nuo Xu, Ruofei Ouyang, Jinqiang Cui, Zhen Zhang and my old friend Yuchen Li. I learnt a lot from them.

I would like to thank NUS Graduate School of Integrative of Science and Engineering for providing me the scholarship, and NUS UAV group for the experimental facilities.

I have a happy family since I was born. I am greatly indebted to my parents, Zhiliang Lan and Meiling Yang, for their unconditional love. I also very grateful to other family members for their support in general. Last but not least, to my beloved wife, Yuwei Jin, who is always nourishing my life with her understanding and encouragement.

Abstract

Compared with handheld cameras widely used today, a camera mounted on a flying drone affords the user much greater freedom in finding the *point of view* (POV) for a perfect photo shot. In the future, many people may take along compact flying cameras, and use their touchscreen mobile devices as viewfinders to take photos. To make this dream come true, the interface for photo-taking using flying cameras has to provide a satisfactory user experience.

In this thesis, we aim to develop a touch-based interactive system for photo-taking using flying cameras, which investigates both the user interaction design and system implementation issues. For interaction design, we propose a novel two-stage *explore-and-compose* paradigm. In the first stage, the user explores the *photo space* to take exploratory photos through autonomous drone flying. In the second stage, the user restores a selected POV with the help of a gallery preview and uses intuitive touch gestures to refine the POV and compose a final photo. For system implementation, we study two technical problems and integrate them into the system development: (1) the underlying POV search problem for photo composition using intuitive touch gestures; and (2) the obstacle perception problem for collision avoidance using a monocular camera.

The proposed system has been successfully deployed in indoor, semi-outdoor and limited outdoor environments for photo-taking. We show that our interface enables fast, easy and safe photo-taking experience using a flying camera.

Contents

List of Figures

List of Tables

Chapter 1

Introduction

1.1 User Interfaces for Photo-taking

User interfaces for photo-taking evolve together with the new characteristics of camera devices, making photo-taking much easier and quicker. This evolution starts since two centuries ago. In 1826, the first permanent photograph in the history of mankind was taken by Joseph Nicphore Nipce [Gernsheim and Gernsheim, 1969]. The photo was made using an 8-hour exposure on pewter coated with bitumen. Later, in 1839, the Giroux daguerreotype camera (Fig. 1.1a) became the first commercially manufactured camera. It was a double-box design, with a lens fitted to the outer box, and a holder for a focusing screen on the inner box. To take a photo, the user needs to perform many steps. First, slide the inner box to adjust the focusing screen for imagery sharpness. Then, replace the screen with a sensitized plate. Next, release the shutter made by a brass plate in the front of the lens. Finally, wait for 5 to 30 minutes of exposure time. As time goes by, cameras evolve from cumbersome to portable, manual to automated, analog to digital. For instance, the Single-Lens Reflex (SLR) camera mechanisms were invented to enable us to view through the lens and see exactly

(a) (b)

(c) (d)

Figure 1.1: Cameras from the past to the future. (a) Giroux daguerreotype camera, the first commercially manufactured camera. (b) Mode dial on a Digital Single-Lens Reflex (DSLR) camera. (c) Photo-taking application on a mobile phone. (d) Parrot Bebop flying camera.

what will be captured, which greatly increased the chance of taking good photos. In addition, the mode dials (Fig. 1.1b) used in most Digital Single-Lens Reflex (DSLR) cameras today allow us to quickly change the camera settings according to different photo-taking scenarios. Furthermore, the mobile phone cameras reduce our efforts on taking a shot and require only a single button click (Fig. 1.1c).

These improvements on camera user interfaces make photo-taking a common daily activity. However, traditional hand-held cameras require human to carry around while finding the *point of view* (POV) for a perfect photo shot, which inherently

limits the cameras' physical reachability and viewpoint coverage. This limitation can be overcome using a flying camera, i.e., a camera mounted on a flying platform (Fig. 1.1d). In this thesis, we aim to further elevate the usability of cameras with the new flying capability.

1.2 Flying Camera Photography

Taking photos with a flying device is not a new concept. As early as the 1860s, balloons, kites and trained pigeons were used to carry cameras for airborne photography. Later, in the early 1900s, airplanes and dirigibles were invented and used. Today, with the advances of miniaturized flying drones, flying cameras are no longer exclusive to the professional users. In the future, many people may take along compact flying cameras, and use their touchscreen mobile devices as viewfinders to compose favorable shots. Although many drone related accessories and gadgets are available in the commercial market, such as combining a joystick with a virtual reality headset to support a firstperson shooter experience, we envision that using a flying camera shall be as easy and natural as using a mobile phone camera today. This thesis proposes a touch-based prototype flying camera interface based on a Parrot Bebop quadcopter (Fig. 1.1d).

Our envisioned flying camera is conceptually not a drone fitted with a camera, but a camera with flying capability. The difference between the two lies in their mental models of interaction. The former implies a model of interacting with two separate devices, a drone, and a camera. The user first pilots the drone painstakingly through a joystick or an emulated joystick interface on a touchscreen (Fig. 1.2a) in order to reach a desired POV, and then operates the camera to take a photo. Most drone-mounted cameras today adopt this model. By contrast, we seek a unified interaction model for a camera capable of flying. The details of drone control are transparent to

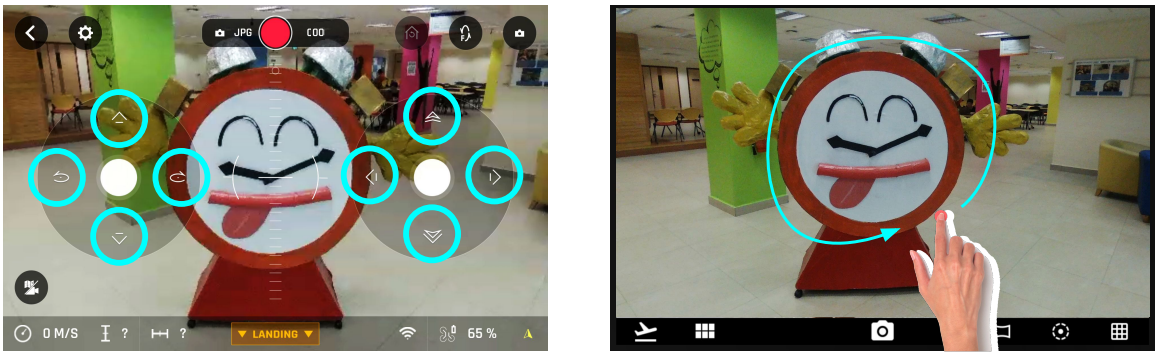

(a) (b)

Figure 1.2: Compare a common joystick interface and XPose. (a) The left joystick controls the drone's heading direction and altitude. The right joystick controls its translational movement along or orthogonal to the heading direction. (b) With XPose, the user interacts directly with the image contents, such as selecting an object of interest by drawing a circle.

the user, making the flying camera more intuitive and easier to use. To realize such a unified interaction model for photo-taking, we introduce the concept of *photo space*. It is defined as the collection of all possible photographs taken for a target scene. Photo-taking becomes a searching problem that looks for a small set of camera views in the entire photo space. In this thesis, we assume the scene is static or almost static, which covers many genres of photography, such as architectural, still life, portrait scenic, etc. Furthermore, we assume each POV produces a unique photo. In other words, each photo is determined only by the camera's extrinsic parameters that define the camera's poses. It is not critical to consider the intrinsic parameters or the internal settings, such as focal length, camera distortion, frame shape and filter style, since those effects can be achieved easily during the post-production process using an image editing software, such as Photoshop.

The development of an interactive system is challenging. The challenges lie in the interplay between interaction design and system implementation. From the interaction design perspective, efficiently searching the infinite photo space is a hard problem in itself. From the system implementation perspective, a light-weight drone

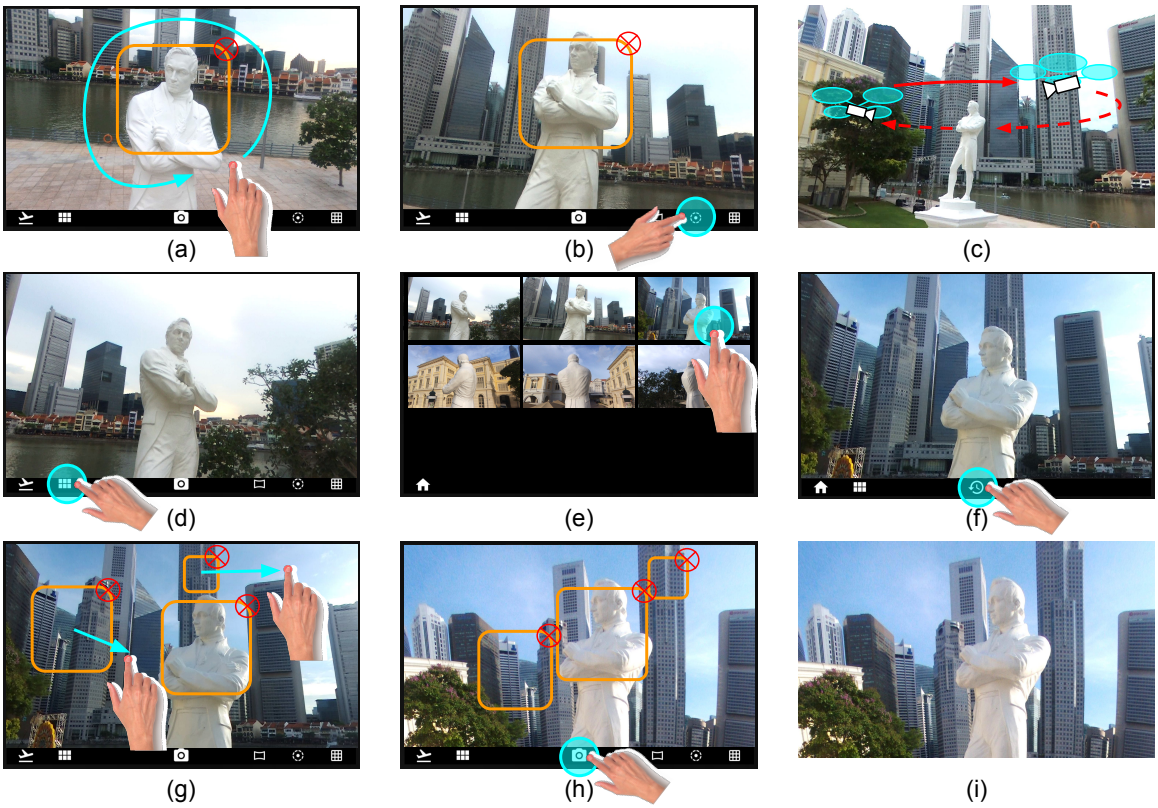

Figure 1.3: An envisioned use case of XPose. (a) Select an object of interest with the encircle gesture. (b) Activate the *Orbit* exploration mode. (c) The drone-mounted camera takes sample photos while orbiting the object of interest autonomously. (d) Enter the gallery preview. (e) Browse sample photos in the gallery. (f) Restore a POV associated with a selected sample photo. (g) Compose a final shot by dragging selected objects of interest to desired locations in the photo. (h) Take the final shot. (i) The final photo.

such as the Parrot Bebop has a severe restriction on the payload and carries only a single forward-facing main camera with a very limited field of view. With a single monocular camera, the system needs to localize the camera with respect to objects of interest, track objects reliably, and avoid collision with obstacles.

We present a touch-based interactive system, named XPose, which investigates both the user interaction design and system implementation issues. For interaction design, XPose proposes a novel two-stage *eXplore-and-comPose* paradigm for efficient and intuitive photo-taking. In the *explore* stage, the user first selects objects of inter-

est (Fig. 1.3a) and the interaction mode (*Orbit*, *Pano*, and *Zigzag*) on a touchscreen interface (Fig. 1.3b). The camera then flies autonomously along predefined trajectories and visits many POVs to take exploratory photos (Fig. 1.3c). The sample photos are presented as a gallery preview (Fig. 1.3d,e). The user taps on a potentially interesting preview photo and directs the drone to revisit the associated POV in order to finalize it (Fig. 1.3f). In the *compose* stage, the user composes the final photo on the touchscreen, using familiar dragging gestures (Fig. 1.3g). The camera flies autonomously to a desired POV (Fig. 1.3h), instead of relying on the user to pilot manually.

Based on the design requirements in the explore-and-compose paradigm, we identify seven main system components for system implementation: gesture recognition, camera localization, object tracking, photo composition, trajectory planning, collision avoidance, and drone control. In the context of flying camera photography, the problems of photo composition and collision avoidance are crucial. In this thesis, we further investigate these two system components. More specifically, we study the underlying POV selection problem for photo composition using intuitive touch gestures, and the obstacle perception problem for collision avoidance using a monocular camera.

In summary, we integrate interaction design and flying camera autonomy to provide an intuitive touch interface so that the user interacts with photos directly and focuses on photo-taking instead of drone piloting.

1.3 User Interactions for POV Navigation

POV navigation can be achieved by manipulating the camera pose and/or interacting with the camera view.Based on the modalities, we categorize different user interactions into *device-centric* techniques and *view-centric* techniques (Fig. 1.4). Device-

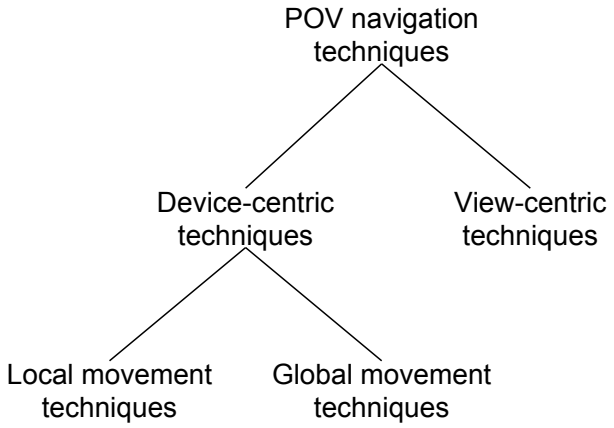

Figure 1.4: POV navigation technique classification.

centric techniques focus more on manipulating the device pose, while view-centric techniques focus more on showing a user intended image view. In the context of photography, view-centric techniques are more preferable over device-centric techniques. It is more intuitive to specify how the view looks like than figuring out which camera pose produces such a view. However, device-centric techniques are dominantly used today on both hand-held and flying cameras. Using hand-held cameras, the user has to manipulate their poses, as they inherently do not have the capability of moving themselves. Flying cameras are essentially flying robots, so device-centric techniques are relatively easy to implement, which is as common as teleoperating other robots with remote controllers.

1.3.1 Device-centric Techniques

Device-centric techniques can be further subdivided into techniques for *local* and *global* movements (Fig. 1.4). Their difference lies in the amount of information required from the environment. Local movements require no or very limited information, while global movements require structural information from the environment.

Local Movement Techniques Local movements usually refer to pan, tilt, dolly, truck and pedestal camera motions. Photographers with hand-held cameras practice these local movements unintentionally. These camera motions have been transferred into the virtual environment to navigate a POV via walking/driving/flying metaphors [Ware and Osborne, 1990; Bowman *et al.*, 1997]. For consumer drones fitted with cameras, the most common interface for POV navigation is probably a touchscreen with emulated joysticks (Fig. 1.2a). The user watches a live video feed from the drone-mounted camera and commands the drone to perform local movements through the joysticks. This approach, which combines joysticks and live video feedback, is also common for teleoperation of remote vehicles [Ballou, 2001; Hainsworth, 2001]. Experiences there suggest that manual control through the joysticks faces several difficulties. The low-level motion control afforded by the joysticks is tedious. Further, operating the drone through only the video feed often results in loss of situational awareness, inaccurate attitude judgment, and failure to detect obstacles [McGovern, 1991].

Another commonly used local movement is rotate (also referred to as orbit, tumble or sweep), which is a standard technique for inspecting a target in the virtual environment, such as Autodesk's 3DS MAX and Maya. The rotate movement only requires the target position to determine the center of rotation and remain a constant distance to it. This is easily obtained in the virtual environment. Similarly, GPS tracking devices [Lily-Next-Gen, 2017] are widely used to enable the flying camera's orbiting movement. However, the GPS may be unavailable or unreliable in indoor environments and urban canyons. Further, GPS maps do not supply the visual information required by the user to identify attractive POVs for photo composition. Besides GPS, image-based tracking algorithms [Skydio-R1, 2018] are used as well. However, existing image-based tracking algorithms are not robust against large viewing angle changes in the process of orbiting around [Kalal *et al.*, 2012].

Global Movement Techniques Global movements specify camera poses using structural information of the environment. Commonly used structural information is a coordinate system or a map. In virtual environments, the user can specify a precise camera pose in the global coordinate. Similarly, GPS satellite map is used to guide drones to fly to particular GPS locations [DJI, 2018a; Bebop, 2018].

Another way to use structural information is to guide the camera movement by constraining its motion. For example, virtual tours have been created in virtual environments. The camera moves along a predefined trajectory automatically while allowing users to deviate locally form the tour [Galyean, 1995; Elmqvist *et al.*, 2008]. Such a tour is conceptually a 1-dimensional constraint. A 2-dimensional constraint is called a "guide manifold" [Hanson and Wernert, 1997; Burtnyk *et al.*, 2002; Khan *et al.*, 2005] that constrains the camera movement along some specially designed 2-dimensional subspace. Constraining the motion of a flying camera has been realized through a decoupled plan-and-execute paradigm [Joubert *et al.*, 2015; Gebhardt *et al.*, 2016]. POV trajectory planning occurs offline and relies on a given 3D virtual model of the real-world environment. Then, the drone carries the camera to execute the planned trajectory. This decoupled plan-and-execute paradigm implies a slow interaction cycle and is not quite suitable for photo-taking in real-time. Moreover, the acquisition of accurate 3D models is also a major challenge in itself and remains an active area of research [Fuentes-Pacheco *et al.*, 2012; Marder-Eppstein, 2016].

1.3.2 View-centric Techniques

As aforementioned, photo-taking using view-centric techniques is more intuitive than using device-centric techniques. Unfortunately, view-centric techniques for photography have not been drawn much attention. Nevertheless, many view-centric techniques have been studied and applied to the virtual camera that is similar to the flying

camera in many aspects. They both can hover in the space and move agilely and autonomously. It is worthy to notice that many device-centric techniques have been applied to both the virtual camera and the flying camera due to their similarities.

View-centric techniques move a POV autonomously based on user intent. A common approach is to communicate user intent with respect to a point of interest (POI). Estimating a user intended POV with respect to a POI was firstly proposed in the Point of Interest Logarithmic Flight technique [Mackinlay *et al.*, 1990] that moves the virtual camera towards and face the POI. Instead of directly facing the POI, UniCam [Zeleznik and Forsberg, 1999] proposes to estimate the camera orientation according to the proximity of the edges of some objects. Rather than estimating a user intended POV, Navidget [Hachet *et al.*, 2008] provides direct and real-time visual feedback using a 3D widget coupled with a preview window so that the user can select a POV while moving a cursor on the 3D widget.

Another view-centric technique is to manipulate the screen-space projection of a scene in the camera view directly, i.e., direct manipulation. Direct manipulation in screen-space [Gleicher and Witkin, 1992; Reisman *et al.*, 2009; Walther-Franks *et al.*, 2011] allows the user to specify desired object positions on the screen. The virtual camera is autonomously controlled so that the selected objects on the screen always stick to the corresponding device pointers, for example, fingertips. A different but related application of direct view manipulation is video browsing [Satou *et al.*, 1999; Dragicevic *et al.*, 2008; Karrer *et al.*, 2008]. Since a video can be seen as a sequence of camera views produced by a fixed trajectory of camera poses, a desired camera view can be found by directly dragging the objects in the video content.

View-centric techniques developed for virtual cameras cannot be directly applied to physical flying cameras. Their fundamental difference lies in their moving speeds, which greatly affects their feedback cycles. In the virtual environment, the user interface is able to respond to rapid user inputs. In particular, the 3D widget of

Navidget corresponds to a collection of all possible views with respect to the target. When the mouse cursor moves on the virtual widget, the corresponding camera view is rendered in the preview window in real-time. By contrast, the physical flying camera cannot afford to provide real-time visual feedback with such a rapid rate, because the camera has to physically fly from one POV to another with limited traveling speed.

In this thesis, we propose the explore-and-compose paradigm, a view-centric POV navigation technique for flying camera photography. Furthermore, we investigate the complete interactive system that aids the user for real-time photo-taking without a 3D model given *a priori*.

1.4 Outline

The rest of the thesis is organized as follows.

Chapter 2 presents the system design. First, we start with an interview study with photographers and drone flyers to understand the design objective and introduce the two-stage explore-and-compose paradigm in detail. Then, we analyze the main system functions in the interactive paradigm and identify the required main system components to implement each function.

Among the main system components, photo composition (Chap. 3) and collision avoidance (Chap. 4) are crucial in the context of flying camera photo-taking. We further investigate them respectively. In Chapter 3, we investigate the underlying POV search problem for photo composition using intuitive touch gestures. We focus on a common situation in photo-taking, i.e., composing a photo with two objects of interest. We model it as a Perspective-2-Point problem, formulate a constrained nonlinear optimization problem, and solve it in closed form. Experiments on both synthetic datasets and the Parrot Bebop flying camera are reported. In addition, we propose a sample-based POV search method for composing a photo with three or

more objects of interest. Next, in Chapter 4, we investigate the obstacle perception problem for collision avoidance using monocular cameras. To perceive obstacles, we propose an algorithm to estimate a dense and accurate depth map for each image frame, which combines the strengths of both the geometry-based approach and the data-driven approach to depth estimation. Our depth map estimation algorithm is evaluated with datasets of real images, and implemented for collision-free path planning with the Parrot Bebop flying camera.

Chapter 5 and Chapter 6 present the system implementation and evaluation respectively. Chapter 5 shows the implementation details of the main system components. Chapter 6 reports the evaluation results for both interaction design and system performance on photo-taking tasks.

Finally, in Chapter 7, we summarize the main results and point out directions for future research.

Chapter 2

System Design

Flying cameras have produced extraordinary photos, with POVs rarely reachable otherwise [Dronestagram, 2017], and endeared themselves to amateur and professional photographers alike. While today flying cameras remain the toys of hobbyists, in the future many people may carry compact drones in pockets [AirSelfie, 2018] or even wear them on the wrists [Flynixie, 2018]. They release the drones into the sky for photo-taking and use their touchscreen mobile phones as viewfinders. This chapter presents the overall design of the flying camera we dreamed of, with the goal of investigating the underlying user interaction design and system implementation issues.

To explore the interaction design requirements, we started with an interview study with photographers and drone flyers (Sec. 2.1.1), and identified the main objective of helping the user to explore POVs efficiently while avoiding the perception of latency when the camera transitions between POVs. We propose the novel two-stage explore-and-compose paradigm that was briefly introduced in Sec. 1.2, which is described with more details later, in Sec. 2.1.

Further, to realize the proposed explore-and-compose design paradigm, XPose is implemented based on the Parrot Bebop quadcopter. The interactive system consists

of seven main components conceptually (Sec. 2.2): gesture recognition, camera localization, object tracking, photo composition, trajectory planning, collision avoidance, and drone control.

In this chapter, we show the details of the system design for both user interaction (Sec. 2.1) and system components (Sec. 2.2). In the end, we discuss the problems encountered in the system implementation life-cycle and the choices made.

2.1 User Interaction

2.1.1 Interview Study

To explore the requirements of effective user interactions with a flying camera, we conducted in-depth semi-structured interviews. The group of interviewees consists of 8 photographers (3 professional and 5 amateur) and 2 professional drone flyers/instructors. They are recruited via social network referrals. For photographers, our questions focused on their main considerations when taking photos and how drone-mounted cameras can potentially help. For drone flyers/instructors, our questions focused on their experience with using drones for photo/video taking and how they train novice users. Each interview session lasted from 30 minutes to an hour. All interviews were transcribed into text for qualitative analysis. We briefly show our findings below.

2.1.1.1 Opportunities for flying cameras

Both the professional photographers and the photography hobbyists mentioned a similar set of important aspects in photo-taking, including POV, lighting, visual composition, and the choice of equipment (with different focal features, shutter speeds, etc.), post-editing and so on.

In terms of how a drone can help them taking photos, all professional photographers point out the potential for drones to find and discover interesting POVs that are normally difficult to reach.

P1, is a professional bird photographer, envisioned the help from a drone to identifying unblocking viewpoint of a bird hidden in trees, which will be much easier and safer approaching than using ladders or climbing trees.

P2, who loves to explore nature, suggested that the drone can be an effective tool to explore the possible POVs in a relatively complex landscape such as in the mountain or valley where there are many barriers that block the view.

P3, the only professional photographer with drone flying experience, commented that drones can be very useful to take photos of very large objects, such as houses, churches, boats. In addition, he mentioned that manually controlling drone while trying to take photos can be a difficult task.

In addition to the suggestions by the professionals, the hobbyists have also made a few interesting suggestions, including taking selfies for a large group of people, taking travel photos of a subject of interest in tourist scenes from a higher angle to avoid unwanted trespassing tourists, etc.

2.1.1.2 Challenges with existing flying cameras user interfaces

As an expert drone photographer, P4 explained that the current common practice follows a decoupled plan-and-execute paradigm (Sec. 1.3.1). To take a photo, the first step is to pre-program a flight plan using a GPS map. While the drone is executing the flight plan, its onboard camera's orientation is manually controlled using a joystick. However, this is not easy as the drone pilot has no visual overview of the scene before the drone arrives.

The lack of a visual overview is caused by two factors. First, the onboard camera offers a narrow field of view, limiting the photographers ability to comprehend the

scene. Second, the aerial scene can only be viewed during the flight, and not before. Conducting reconnaissance (preliminary visual scouting) for an aerial is far more challenging than reconnoitering for a shot on the ground because of these two factors. Therefore, taking photos with drones involves many unsuccessful attempts since it can be difficult to previsualize what the photo will look like.

In addition, pre-programming and manual control can be tedious and complex. A professional drone usually requires sophisticated pre-programming procedures and many degrees-of-freedom of manual controls. Furthermore, some professional drones even require two operators using two separate sets of joysticks to control a single drone. One takes charge of drone flying, and the other focuses on photo/video taking [DJI, 2018b].

P4 also pointed out some practical limitations of drones. Unfortunately, a photographers photo-taking time is limited by the drone's battery power. Usually, the pilot only has a handful number of flight attempts before the drone must be returned for recharging. This means that the appropriate POV for a desired shot must again be found during the next attempt. To increase the likelihood of success, drone photographers carefully pre-program the flight plan before flying the drone. Being a proficient pilot helps to reduce errors in piloting the drone and increase the chance of taking better photos.

However, learning to pilot a drone professionally is not an easy task. A significant amount of training is required. P5 is a drone pilot trainer who described the typical training program he conducts to us. He typically runs an introductory course that lasts for two days. The first day has five one-hour sessions to learn how drones work, how to use joysticks and how to use the flight training simulator. On the second day, the trainees practice flying under the tutelage of the trainers. Learners first learn from flying with the simulators. However, even after hours of training on the simulator, most novices will still crash their drones during a real practice. Both P4

and P5 mentioned that it took them about one year of frequent practice to achieve their current proficiency levels.

2.1.1.3 Summary

In summary, the photographers' responses suggest a set of well-established considerations for photo-taking: POVs, visual composition, lighting conditions, shutter speed, depth of field, etc. They also point to the potential for drone-mounted cameras to discover novel POVs. The drone flyers/instructors' responses include lengthy preparations for drone photo/video taking sessions and extensive training required for novice users. These led to our design objective of a simple, intuitive interface for efficiently exploring many POVs and directly manipulating the visual composition.

2.1.2 Explore-and-Compose

With traditional hand-held cameras, the user explores POVs by moving around and looking through the viewfinder. Limited by the user's physical movements, the exploration of POVs is *local*, but the visual feedback is almost instantaneous. The joystick touchscreen interface tries to reproduce this experience for flying cameras: the joysticks control the camera's local movements, and the touchscreen provides visual feedback. However, this approach does not account for the difference in device characteristics between hand-held cameras and flying cameras. The camera's ability to fly offers the opportunity of exploring POVs more *globally*. At the same time, it is more difficult for a flying camera to achieve an intended POV precisely, due to air disturbance and other factors. Further, visual feedback is not instantaneous, because of the communication delay between the flying camera and the user's mobile device.

We introduce a two-stage explore-and-compose paradigm, which enables the user to explore a wide range of POVs efficiently in a hierarchical manner. In the explore

stage, the user samples many POVs globally at a coarse level, through autonomous drone flying. In the compose stage, the user chooses a sampled POV for further refinement and composes the final photo on the touchscreen by interacting directly with objects of interest in the image.

We now illustrate our approach in detail with a concrete scenario (Fig. 1.3). Our main character, Terry, walks along a river on a sunny day and stops at a white statue. She wishes to take a photo of the statue, but can hardly get a close-up shot with a hand-held camera, as the statue is almost 15 feet in height. Terry launches XPose using the associated app on her mobile device. The home view of the app contains a viewfinder, which displays the live video feed from the drone-mounted camera.

2.1.2.1 Explore

Terry is initially unsure about the best viewing angle for the shot and decides to explore the POVs around the statue. She selects the statue as the object of interest and uses XPose's exploration modes to sample the POVs.

Object of Interest Selection First, Terry performs pan and zoom gestures (Fig. 2.1) on the touchscreen to get the statue into the viewfinder. Then she draws a circle around the statue in the viewfinder (Fig. 1.3a). A rectangular bounding box appears to confirm that the statue has been selected and is being tracked.

POV Sampling While the statue is being tracked in the viewfinder, Terry activates the *Orbit* exploration mode (Fig. 1.3b). The flying camera then takes sample shots while orbiting around the statue autonomously (Fig. 1.3c).

XPose currently provides three explorations modes: *Orbit*, *Pano*, and *Zigzag* (Fig. 2.2). They leverage the autonomous flying capability of a drone-mounted camera and systematically explore the POVs by taking sample shots evenly distributed

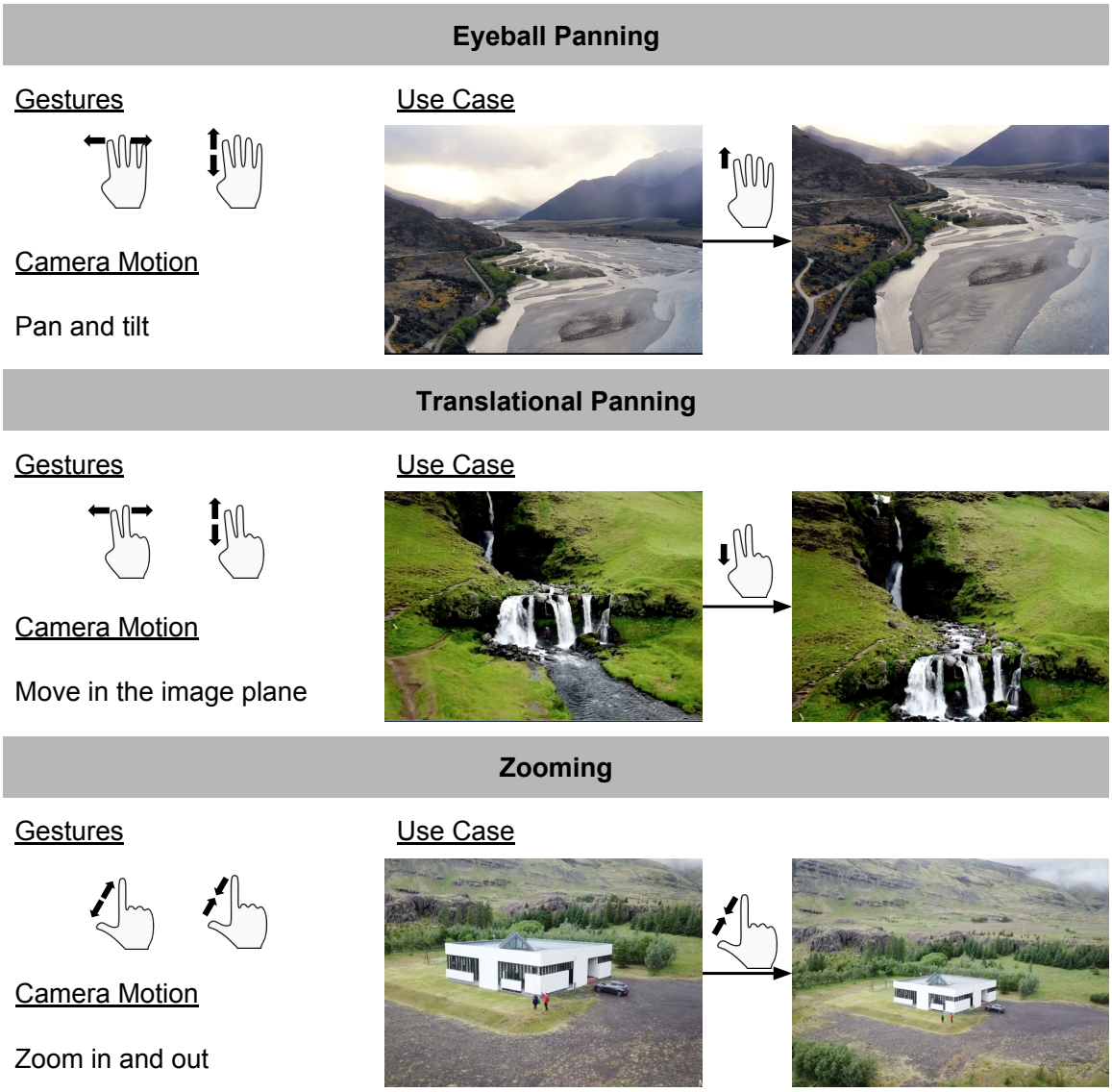

Figure 2.1: User intents for direct view manipulation. User intents of eyeball panning and translation panning are expressed via swiping gestures with four and two fingers respectively. The zooming intents are expressed via pinch and stretch gestures. In addition, single-finger gestures are already reserved for object selection by encircling (Fig. 1.3a) and object composition by dragging (Fig. 1.3g).

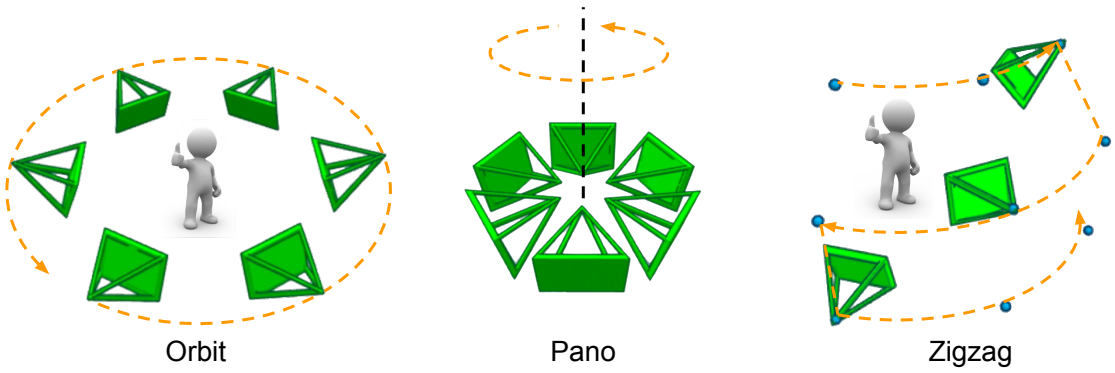

Figure 2.2: Exploration modes.

along predefined trajectories. The Orbit mode is useful when the user has a single main object of interest, e.g., a person, a statue, or an interesting artifact, but is quite unsure about the viewing angle for the best shot. Under this mode, the camera flies a full circle, while looking inward at the object in the center. Under the Pano mode, the camera looks outward, instead of inward. There is no object of interest to be focused. The camera stays at a fixed location while panning horizontally for full 360 degrees. This mode is well-suited for panoramic shots of scenic landscapes, such as oceans, prairies, or glaciers. The Orbit and Pano modes pan the camera, but fix its tilt. The Zigzag mode exploits both panning and tilting. It is useful when the user knows roughly the best viewing angle of an object of interest against its background scene. The camera flies along circular arcs at multiple heights, all centered at the object of interest. Again, the camera always points at the object. One use of the Zigzag mode is to take a selfie against a scenic background. The exploration modes free the user from the tedium of manually piloting the drone through low-level motion commands.

2.1.2.2 Compose

After getting many sample shots through the Orbit mode, Terry is ready to finalize the photo.

POV Restore Terry switches to the gallery view in the app (Fig. 1.3d) and browses the sample shots displayed there (Fig. 1.3e). All sample photos have the statue in the center, but different backgrounds. To take a closer look, Terry taps on a photo to see it in the full-screen photo view (Fig. 1.3e,f). One photo with many tall buildings in the background looks promising, but the composition is not ideal. The accidental alignment of the statue's head and a tall building is distracting. To refine it, Terry taps a button and commands the flying camera to restore the POV associated with the selected sample photo (Fig. 1.3f).

Direct View Manipulation From the restored POV, Terry selects two buildings in the viewfinder as additional objects of interest and drags them, one at a time, to the left and right side of the statue respectively, so that the statue's head appears in the gap between the two buildings (Fig. 1.3g). XPose flies to a new POV that produces the desired composition as closely as possible and displays the photos in the viewfinder. Quite satisfied, Terry takes the final shot (Fig. 1.3h,i).

2.2 System Functions

System functions introduced in the explore-and-compose paradigm are supported by seven system components: gesture recognition, camera localization, object tracking, photo composition, trajectory planning, collision avoidance, and drone control. This subsection shows how the system functions depend on the system components. Tab. 2.1 is an overview.

System Components	Explore		Compose	
	Object of Interest Selection	*POV Sampling*	*POV Restore*	*Direct View Manipulation*
Gesture Recognition	✔			✔
Camera Localization		✔		✔
Object Tracking	✔	✔*		✔*
Photo Composition				✔
Trajectory Planning		✔	✔	✔
Collision Avoidance		✔	✔	✔
Drone Control	✔	✔	✔	✔

Table 2.1: Main functions and system components. ✔indicates a required system component. ✔* indicates that the system component is required when there are selected objects of interest.

2.2.1 Object of Interest Selection

For object selection, the system must recognize the user's gestures: pan, zoom, encircle, etc. For the pan and zoom gestures (Fig. 2.1), the system executes the corresponding camera motions. For the encircle gesture (Fig. 1.3a), the system selects the object and tracks it in the image, as the flying camera moves.

2.2.2 POV Sampling

For POV sampling, the system first plans an exploratory trajectory according to the selected exploration mode and samples the POVs at equal distance along the trajectory. It visits each sampled POV sequentially, takes a photo at the POV, and stores both the image and the camera pose. The system must be localized at all times, in order to check whether a planned POV has been reached. While visiting different POVs, the camera shall avoid colliding with obstacles.

2.2.3 POV Restore

The system keeps track of the POVs of all sample photos obtained in the explore stage. When the user asks to restore the POV of a selected sample photo, the system plans and executes a restoring trajectory until it reaches the designated POV.

2.2.4 Direct View Manipulation

To finalize the composition, the user may select objects of interest and drag them to desired locations in the photo. It then computes the POV that produces the desired composition as closely as possible, plans a trajectory to it, and flies there.

2.3 Discussion

We investigate both the user interaction design and system implementation issues. From the design perspective, our proposed explore-and-compose paradigm aims to achieve the design objective of a more intuitive interface for efficiently exploring POVs and directly manipulating the visual composition. From the implementation perspective, there are many practical problems encountered during the implementation life-cycle.

2.3.1 Problem in Camera Localization

For the camera localization component, there are many simultaneous localization and mapping (SLAM) algorithms available, such as PTAM [Klein and Murray, 2007], SVO [Forster *et al.*, 2014], LSD-SLAM [Engel *et al.*, 2014a], ORB-SLAM[Mur-Artal *et al.*, 2015] and so on. PTAM, as one of the pioneer works in monocular camera SLAM, is designed for the use case of augmented reality in small workspaces. There are a few limitations preventing PTAM from being used in the photo-taking

setting. In particular, PTAM can hardly localize the camera while building a large map during exploration, because PTAM runs a full bundle adjustment which limits its scale to small workspaces [Strasdat *et al.*, 2011]. SVO, the first version [Forster *et al.*, 2014], assumes an almost planar environment. It works well for a downward-looking camera, but is not the ideal choice for localizing a forward-facing camera on the Parrot Bebop drone. SVO2 [Forster *et al.*, 2017] removes this assumption. LSD-SLAM localizes the camera by comparing the entire images to each other to reference them to each other, which is not robust against outliers. Unfortunately, the drone-mounted camera suffers from poor image quality and frequent frame dropping due to limited onboard processing power and unstable wireless connection, so that LSD-SLAM is not a reliable choice. Finally, ORB-SLAM became our choice in the prototype implementation. It employs the concept of *covisibility* [Mei *et al.*, 2010; Strasdat *et al.*, 2011] to enable exploration in large environment. Moreover, ORB-SLAM localizes the camera by exacting corner features from each frame, which makes it robust against many practical issues common to drone-mounted cameras, such as temporary frame drops, occlusions, camera exposure changes, etc.

2.3.2 Problem in Object Tracking

For the object tracking component, an image-based tracking algorithm [Kalal *et al.*, 2012; Nebehay and Pflugfelder, 2015] seems to be a natural choice. However, existing image-based tracking algorithms are not robust against large viewing angle changes (e.g., in the Orbit mode) or large viewing distance changes (e.g., while zooming in and out). We present our approach to robust object tracking in Sec. 5.2.3.

2.3.3 Problem in Photo Composition

Composition is one of the utmost important aspects of photo-taking. In our design, the system needs to compute the POV that produces the user desired composition. Chapter 3 is dedicated to investigating the underlying POV search problem for composing multiple objects of interest in the scene.

2.3.4 Problem in Collision Avoidance

Last but not least, collision avoidance is a standard but important problem to be addressed for flying drones. Due to the interactive nature of the system design, the system needs to avoid collisions while achieving user intended POVs. In Chapter 4, we present a method that estimates a dense depth map based on monocular camera image input that is then used to reach user intended POVs while avoiding obstacles.

Chapter 3

POV Selection for Photo Composition

Composition in photography refers to the arrangement of visual elements within an image frame. It is critical for a photograph. A well-composed photo conveys a clear message from the photographer to the viewer. Usually, the photographer interprets a group of visual elements as an object of interest in the scene, such as a statue, a crowd of people, a row of buildings in the background, etc. With XPose, the user performs intuitive gestures to directly compose multiple objects of interest on the image plane (Fig. 1.3g,h). This chapter is dedicated to investigating the underlying POV selection problem for composing multiple objects of interest in the scene.

While composing a photo, the photographer decides where each object of interest is located in the viewfinder. We define the composition of a photo as the compositions of all objects of interest. Formally speaking, the composition of each object β is the region it occupies on the image, denoted by $\mathbf{R}_\beta$, and its desired composition is another region $\mathbf{R}^*_\beta$ on the image. We define *composition error* ϵ_{c} as the difference between the actual composition and the desired composition:

$$\epsilon_{\mathrm{c}} = \sum_{\beta \in B} d_{\mathrm{H}}(\mathbf{R}_\beta, \mathbf{R}^*_\beta) \tag{3.1}$$

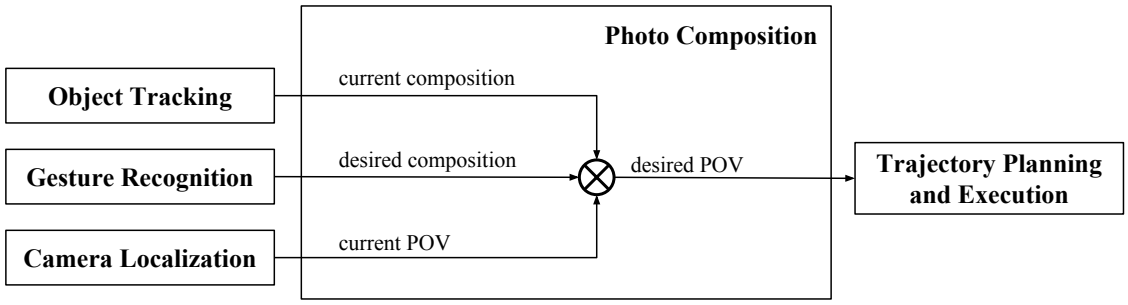

Figure 3.1: Information flow for photo composition component.

where B is the object set and $d_{\mathrm{H}}(\cdot, \cdot)$ is the Hausdorff distance [Rockafellar and Wets, 2009] between two regions. The Hausdorff distance is normalized with respect to the diagonal length of the image. For simplicity, we use the center point of the bounding box as the actual composition location, and the ending point of the dragging gesture as the desired composition location. This simplification makes the Hausdorff distance between two regions to be the Euclidean distance between two points. A photo with the desired composition is the one that minimizes the composition error (Eq. (3.1)).

In order to produce a photo with the desired composition, the flying camera has to place itself at the corresponding desired POV. This is achieved by the photo composition component in our system design (Tab. 2.1). Fig. 3.1 illustrates the information flow for this component. The inputs are the current object composition provided by object tracking, the user desired composition provided by gesture recognition, and the current camera POV provided by camera localization. The output is a POV with desired composition. This POV selection problem is closely related to the well-known Perspective-n-Point (PnP) problem estimating the pose of a calibrated camera given a set of n 3D points in the world and their corresponding 2D projections in the image.

Generally speaking, there are only a handful number of main objects of interest in a photograph. We first focus on the case of composing two objects of interest, a common situation in photo-taking (Sec. 3.1). For example, foreground-background

Figure 3.2: Photos with two main objects of interest.

composition and side-by-side composition are good practices in both hand-held camera photography (Fig. 3.2a,b,c) and flying camera photography (Fig. 3.2d,e,f). To compose more objects of interest, we propose a sampled-based method in Sec. 3.2.

3.1 Two Objects Composition

Assume that the positions of two objects of interest are known and their corresponding projections on the image plane are specified by the user. Determining the 6 DoFs camera pose that satisfies the composition constraints corresponds to the PnP problem with $n = 2$. P2P is related to the family of minimal problems in computer vision, and our solution approach shares a similar line of thought. Many minimal problems in computer vision attempt to solve for the unique solution of the unknown camera parameters with a minimum number of correspondences. In particular, P3P is the minimal problem in the family of PnP problems, which requires $n = 3$ point correspondences. Having only $n = 2$ point correspondences, the P2P problem is

under-determined and has infinite solutions. This means that there are infinitely many photos with the desired composition, i.e., the composition error is zero. We propose to solve the problem by adding the constraint that the flying camera should reach one of the solutions as fast as possible along the shortest path. This leads to a constrained nonlinear optimization problem.

We show that our constrained nonlinear optimization problem can be solved in *closed form*. By analyzing the geometry of the solution space and applying the first-order optimality conditions of the objective function, we derive a maximum of 16 candidate solutions. We then obtain the global optimum by enumeration. While generic nonlinear optimization methods can solve our problem as well, they are not practical onboard the drones that have limited computation power. In addition, they often get stuck in local minima, because of the nonlinear constraints.

In this section, we investigate the P2P problem for flying-camera photo composition (Sec. 3.1.2). We provide a closed-form solution to the resulting constrained nonlinear optimization problem (Sec. 3.1.3). Finally, we conduct experiments on synthetic datasets and on a real flying camera to evaluate our solution for feasibility and robustness (Sec. 3.1.4).

3.1.1 Related Work

Minimal Problems Minimal problems in computer vision are the problems solved from a minimal number of correspondences. For example, in the five-point relative pose problem [Nistér, 2004], five corresponding image points are needed to provide five epipolar equations to estimate the essential matrix. A sixth point correspondence is needed if the focal length is unknown [Stewénius *et al.*, 2008] or there is a radial distortion parameter to be estimated [Byrod *et al.*, 2008; Kukelova and Pajdla, 2007b]. Similarly, additional correspondences are required if there are more un-

known camera parameters, such as the eight-point problem for estimating fundamental matrix and single radial distortion parameter for uncalibrated cameras [Kukelova and Pajdla, 2007a], and the nine-point problem for estimating fundamental matrix and two different distortion parameters for uncalibrated cameras [Byrod *et al.*, 2008; Kukelova and Pajdla, 2007b]. By contrast, we solve for a camera pose with six unknown parameters, but it only has four equations derived from two correspondences.

Perspective-n-Point PnP problems estimate the rotation and translation of a calibrated perspective camera by using n known 3D reference points and their corresponding 2D image projections. Since each correspondence provides two equality constraints, the minimal case is having three correspondences [Gao *et al.*, 2003]. Four and more correspondences have been also investigated to improve the robustness of the solution [Triggs, 1999; Lepetit *et al.*, 2009; Li *et al.*, 2012; Zheng *et al.*, 2013; Urban *et al.*, 2016].

This section solves a P2P problem. Early studies on P2P make additional assumptions, such as planar motion constraints [Booij *et al.*, 2009; Choi and Park, 2015], known camera orientation [Merckel and Nishida, 2008; Bansal and Daniilidis, 2014], known viewing direction and triangulation constraint of the 3D points [Camposeco *et al.*, 2017]. We make no such assumptions. Instead, we form an optimization problem to find the solution with the minimal flying distance to reach.

3.1.2 Problem Formulation

We represent each object as a ball B_j^W, $j = 1, 2$, in a world coordinate frame F_W [1]. The ball center $\mathbf{q}_j^W = [x_j^W, y_j^W, z_j^W]^T$ represents the estimated object centroid position, and the radius ϵ_j denotes a collision-free distance estimated based on the object size

[1] In this chapter, the superscripts, W, I and C, denote the world, image and camera coordinate frames, respectively.

during selection. Compared with other object representations with more details, a ball representation is not only easy for human to interact with, but also efficient in computation [Gleicher and Witkin, 1992; Kyung *et al.*, 1996; Reisman *et al.*, 2009; Lino and Christie, 2015]. For each object, its corresponding user-specified projections on the image plane are represented as $\mathbf{p}_j^I = [u_j^I, v_j^I, 1]^T$ in the homogeneous image coordinate frame F_I. It is worth to notice that the correspondences between $\mathbf{p}_j^I$ and $\mathbf{q}_j^W$ form a P2P problem that is known to have infinitely many solutions.

Among the solutions, we are interested in one camera pose in the world coordinate frame F_W that could be represented as a rotation matrix $\mathbf{R}_C^W$ and a translation vector $\mathbf{t}_C^W$ from the camera coordinate frame F_C to F_W. This particular camera pose should be the nearest one to a given starting camera position $\mathbf{t}_0^W = [x_0^W, y_0^W, z_0^W]^T$ in F_W. Moreover, it should not collide with the two objects of interest. Hence, we formulate an optimization problem as follows.

$$\underset{\mathbf{R}_C^W, \mathbf{t}_C^W}{\operatorname{argmin}} \|\mathbf{t}_C^W - \mathbf{t}_0^W\|^2, \tag{3.2}$$

subject to

$$\lambda_j \mathbf{p}_j^I = \mathbf{K}\ (\mathbf{R}_W^C\ \mathbf{q}_j^W + \mathbf{t}_W^C), \tag{3.3a}$$

$$\|\mathbf{t}_C^W - \mathbf{q}_j^W\| \geq \epsilon_j, \tag{3.3b}$$

in which $j = 1, 2$. λ_j denotes the depth factor of the j-th object. $\mathbf{K}$ is the calibrated intrinsic parameter matrix for the perspective camera with the pinhole imaging model. $\mathbf{R}_W^C$ and $\mathbf{t}_W^C$ denote the rotation matrix and translation vector from F_W to F_C, respectively.

The equality constraint in Eq. (3.3a) corresponds to the projective imaging equations derived from the two point correspondences. Since $\mathbf{K}$ is known, it is convenient

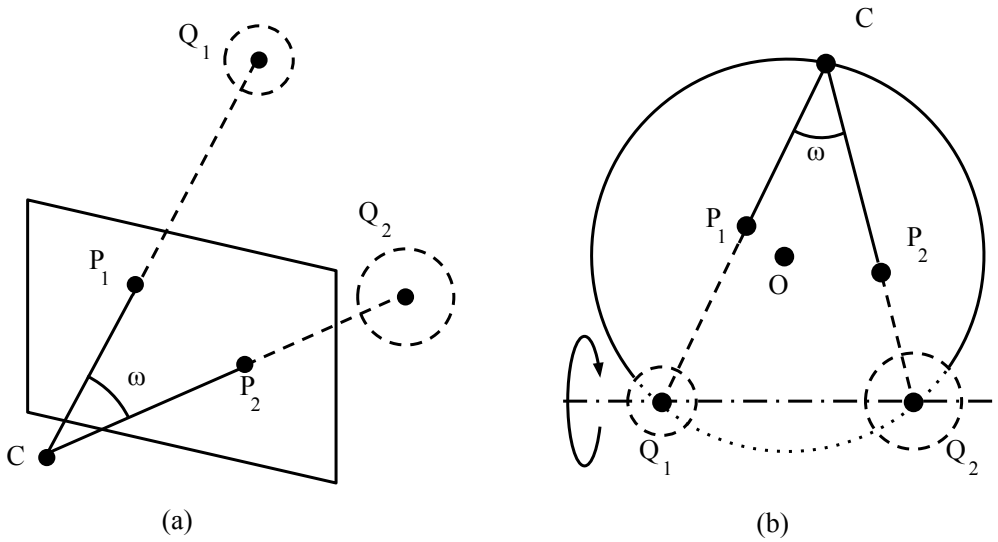

Figure 3.3: Camera positions that satisfy constraints in Eq. (3.3). C denotes the camera's center of perspective. Q_1 and Q_2 denote the object positions. P_1 and P_2 denote the user-specified object projections. (a) $\angle Q_1CQ_2 = \angle P_1CP_2 = \omega$ is a constant angle. (b) All points on the solid arc of $\odot O$ satisfy constraints in Eq. (3.3). Rotating the arc around the axis through Q_1 and Q_2 forms a toroidal surface, on which all points satisfy constraints in Eq. (3.3) as well.

to use the normalized camera coordinate frame

$$\hat{\mathbf{p}}_j^C = [\hat{u}_j \ \hat{v}_j \ 1]^T = \mathbf{K}^{-1} \ \mathbf{p}_j^I, \ j = 1, 2. \tag{3.4}$$

The inequality constraint in Eq. (3.3b) ensures a collision-free distance to each object. It is reasonable to assume that $\epsilon_1 + \epsilon_2$ is relatively small as compared to the distance between the two objects, which, in fact, ensures the existence of the solution.

3.1.3 P2P Solution in Closed Form

Before diving into the details of the algebraic derivation, we first analyze the solution space of the constraints. The solution space for camera positions $\in \mathcal{R}^3$ that satisfy the constraints is a toroidal surface (Fig. 3.3b and 3.4a). Each camera position corresponds to a unique camera orientation $\in SO(3)$, so that we can first solve for

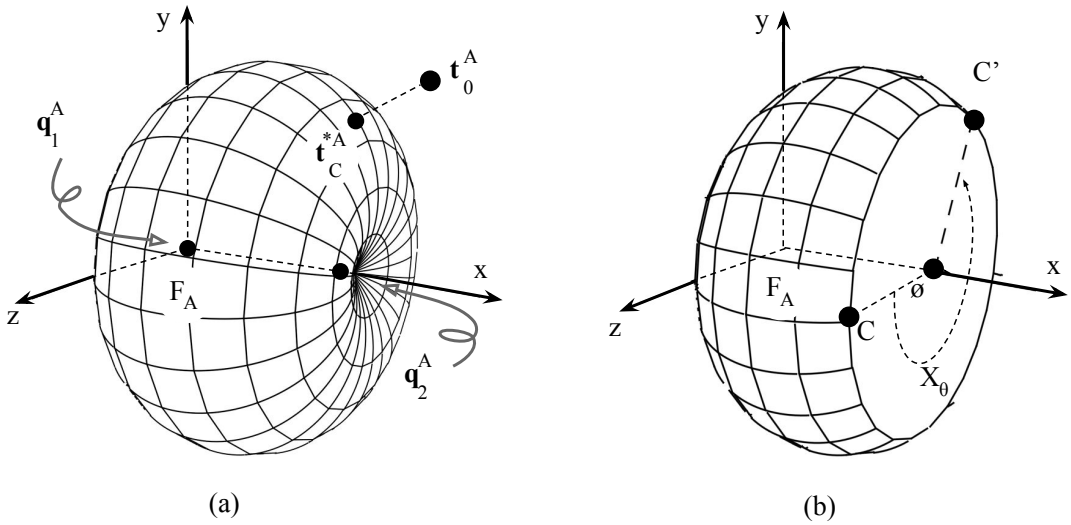

Figure 3.4: The auxiliary frame F_A. (a) The objective is to find $\mathbf{t}^{*A}_C$ on the toroidal surface with the minimal distance to the given starting camera position $\mathbf{t}^A_0$. (b) The intersections between the toroidal surface and any plane $x = x_\theta$ in F_A are circles, so any point C' on the circle can be parametrized using a reference point C and an angle ϕ.

the position and then determine the orientation.

Parameterizing the toroidal solution space $\in \mathcal{R}^3$ is the key to solve the problem. The toroid surface has 2 DoFs: the arc and the rotational axis as shown in Fig. 3.3b. We introduce an auxiliary frame with one axis passing through the rotational axis of the toroid for easy parameterization.

Next, we solve the optimization problem with the following steps. First, we construct the auxiliary coordinate frame. Then, we reformulate the constraints and the objective function using the auxiliary frame. Finally, we solve the equation system derived from the first-order optimal condition of the objective function to find the global optimal camera position, hence, the corresponding camera orientation.

3.1.3.1 Constructing the Auxiliary Frame

We construct the auxiliary frame F_A with one axis be the axis of rotation passing through $\mathbf{q}_1^W$ and $\mathbf{q}_2^W$ as shown in Fig. 3.3. More specifically, $\mathbf{q}_1^W$ coincides with the origin of F_A and $\mathbf{q}_2^W$ sits on the positive x-axis of F_A (Fig. 3.4a), i.e.,

$$\mathbf{q}_1^A = \begin{bmatrix} 0 \\ 0 \\ 0 \end{bmatrix}, \quad \mathbf{q}_2^A = \begin{bmatrix} \xi_{len} \\ 0 \\ 0 \end{bmatrix}, \quad \xi_{len} = \|\mathbf{q}_1^W - \mathbf{q}_2^W\|. \tag{3.5}$$

Using the auxiliary frame, we manage to reformulate and solve the original problem in a simpler form, as shown later from Sec. 3.1.3.2 to Sec. 3.1.3.7.

Let $\mathbf{R}_A^W$ and $\mathbf{t}_A^W$ be the rotation matrix and translation vector from F_A to F_W, respectively. Then, $\mathbf{t}_A^W = \mathbf{q}_1^W$, and the first column of $\mathbf{R}_A^W$, $\mathbf{c_1}_A^W = (\mathbf{q}_2^W - \mathbf{q}_1^W)/\xi_{len}$. The second and the third columns of $\mathbf{R}_A^W$ could be chosen as an arbitrary pair of orthonormal vectors that span the null space of $\mathbf{c_1}_A^W$. In the case when $\mathbf{R}_A^W$ is an improper rotation matrix, i.e., $\det(\mathbf{R}_A^W) = -1$, we swap the second and the third columns of $\mathbf{R}_A^W$.

3.1.3.2 Reformulating Equality Constraints

Now, we use the auxiliary frame F_A to reformulate the equality constraints in Eq. (3.3a),

$$\lambda_j \hat{\mathbf{p}}_j^C = \mathbf{R}_A^C \ \mathbf{q}_j^A + \mathbf{t}_A^C, \ j = 1, 2, \tag{3.6}$$

in which $\mathbf{R}_A^C$ and $\mathbf{t}_A^C$ are the unknown rotation matrix and translation vector from F_A to F_C,

$$\mathbf{R}_A^C = \begin{bmatrix} r_{11} & r_{12} & r_{13} \\ r_{21} & r_{22} & r_{23} \\ r_{31} & r_{32} & r_{33} \end{bmatrix}, \quad \mathbf{t}_A^C = \begin{bmatrix} t_1 \\ t_2 \\ t_3 \end{bmatrix}. \tag{3.7}$$

Next, it is desirable to eliminate the depth factors as follows,

$$[\hat{\mathbf{p}}_j^C]_\times \ (\mathbf{R}_A^C \ \mathbf{q}_j^A + \mathbf{t}_A^C) = \mathbf{0}_{3\times 1}, \ j = 1, 2, \tag{3.8}$$

where $[\hat{\mathbf{p}}_j^C]_\times$ is the skew-symmetric matrix for vector $\hat{\mathbf{p}}_j^C$. Eq. (3.8) produces six equality constraints, and two of them are redundant. We transform the remaining four equality constraints into a matrix form,

$$\mathbf{A} \ \mathbf{w} = \mathbf{0}_{4\times 1}, \tag{3.9}$$

where

$$\mathbf{A} = \begin{bmatrix} 0 & 0 & 0 & 0 & -1 & \hat{v}_1 \\ 0 & 0 & 0 & 1 & 0 & -\hat{u}_1 \\ 0 & -1 & \hat{v}_2 & 0 & -1/\xi_{len} & \hat{v}_2/\xi_{len} \\ 1 & 0 & -\hat{u}_2 & 1/\xi_{len} & 0 & -\hat{u}_2/\xi_{len} \end{bmatrix}, \quad \mathbf{w} = \begin{bmatrix} r_{11} \\ r_{21} \\ r_{31} \\ t_1 \\ t_2 \\ t_3 \end{bmatrix}, \tag{3.10}$$

in which r_{11}, r_{21}, r_{31}, t_1, t_2 and t_3 are the entries in $\mathbf{R}_A^C$ and $\mathbf{t}_A^C$ defined above. Note that there is a constraint imposed on the first three entries, r_{11}, r_{21} and r_{31}, in $\mathbf{w}$, as they form the first column $\mathbf{c_1}_A^C$ of $\mathbf{R}_A^C$, which means $\|\mathbf{c_1}_A^C\| = 1$.

The benefit of constructing F_A shows up. Since $\mathbf{q}_1^A$ and $\mathbf{q}_2^A$ are constructed to have only one non-zero entry, $\mathbf{w}$ is much simplified so that it does not contain the entries in the second column $\mathbf{c_2}_A^C$ and the third column $\mathbf{c_3}_A^C$ of $\mathbf{R}_A^C$. Otherwise, without F_A, $\mathbf{w}$ would contain all the 9 entries in a rotation matrix with more constraints imposed.

Next, we parameterize $\mathbf{w}$. The vector $\mathbf{w}$ of unknowns belongs to the null space of $\mathbf{A}$. Since $\mathit{nullity}(\mathbf{A}) = 2$ as $\mathit{rank}(\mathbf{A}) = 4$ according to Eq. (3.10), $\mathbf{w}$ can be expressed

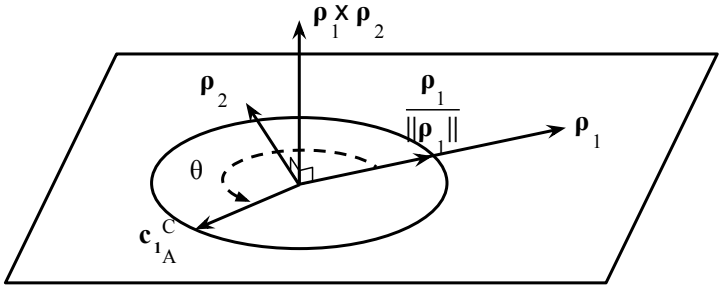

Figure 3.5: Parameterization of $\mathbf{c_1}_A^C$ using θ.

as the following linear combination form,

$$\mathbf{w} = \begin{bmatrix} \mathbf{e}_1 & \mathbf{e}_2 \end{bmatrix} \begin{bmatrix} \alpha_1 \\ \alpha_2 \end{bmatrix}, \quad \mathbf{e}_1 = \begin{bmatrix} \hat{u}_2 \\ \hat{v}_2 \\ 1 \\ 0 \\ 0 \\ 0 \end{bmatrix}, \ \mathbf{e}_2 = \begin{bmatrix} \hat{u}_2 - \hat{u}_1 \\ \hat{v}_2 - \hat{v}_1 \\ 0 \\ \hat{u}_1 \xi_{len} \\ \hat{v}_1 \xi_{len} \\ \xi_{len} \end{bmatrix}, \tag{3.11}$$

where α_1 and α_2 are two coefficients, $\mathbf{e}_1$ and $\mathbf{e}_2$ are the two eigenvectors of $\mathbf{A}$ corresponding to the two null eigenvalues of $\mathbf{A}$, which could be easily verified. Hence, $\mathbf{c_1}_A^C$ and $\mathbf{t}_A^C$ can be expressed as linear combinations as well,

$$\mathbf{c_1}_A^C = \begin{bmatrix} \boldsymbol{\rho}_1 & \boldsymbol{\rho}_2 \end{bmatrix} \begin{bmatrix} \alpha_1 \\ \alpha_2 \end{bmatrix}, \quad \mathbf{t}_A^C = \begin{bmatrix} \boldsymbol{\tau}_1 & \boldsymbol{\tau}_2 \end{bmatrix} \begin{bmatrix} \alpha_1 \\ \alpha_2 \end{bmatrix}, \tag{3.12}$$

in which $\boldsymbol{\rho}_1 = \hat{\mathbf{p}}_2^C$, $\boldsymbol{\rho}_2 = \hat{\mathbf{p}}_2^C - \hat{\mathbf{p}}_1^C$, $\boldsymbol{\tau}_1 = \mathbf{0}_{3\times 1}$ and $\boldsymbol{\tau}_2 = \hat{\mathbf{p}}_1^C \xi_{len}$.

Now, $\mathbf{c_1}_A^C$ and $\mathbf{t}_A^C$ are parameterized with two parameters, α_1 and α_2. Next, we use the constraint, $\|\mathbf{c_1}_A^C\| = 1$, to reduce to a form using only one parameter. The idea is depicted in Fig. 3.5. We observe that $\mathbf{c_1}_A^C$ is a unit vector in the 2D plane spanned by $\boldsymbol{\rho}_1$ and $\boldsymbol{\rho}_2$. Hence, it can be parameterized using a rotation angle θ. We

denote the matrix for a rotation by an angle of θ around $\boldsymbol{\rho}_1 \times \boldsymbol{\rho}_2$ as $\mathbf{R}_\theta$. Hence, ${\mathbf{c_1}}_A^C = \mathbf{R}_\theta \boldsymbol{\rho}_1 / \|\boldsymbol{\rho}_1\|$, which contains θ as the only parameter. More explicitly,

$$ {\mathbf{c_1}}_A^C = \sin(\theta) \begin{bmatrix} \xi_1 \\ \xi_2 \\ \xi_3 \end{bmatrix} + \cos(\theta) \begin{bmatrix} \xi_4 \\ \xi_5 \\ \xi_6 \end{bmatrix}, \tag{3.13} $$

in which ξ_k's are constant, $k = 1, 2, 3, 4, 5, 6$, i.e.,

$$ \begin{aligned} \xi_1 &= \frac{-\hat{u}_1 + \hat{u}_2 + \hat{u}_2\hat{v}_1\hat{v}_2 - \hat{u}_1\hat{v}_2^2}{\|\boldsymbol{\rho}_1\|\|\boldsymbol{\rho}_1 \times \boldsymbol{\rho}_2\|}, & \xi_4 &= \frac{\hat{u}_2}{\|\boldsymbol{\rho}_1\|}, \\ \xi_2 &= \frac{-\hat{v}_1 + \hat{v}_2 + \hat{v}_2\hat{u}_1\hat{u}_2 - \hat{v}_1\hat{u}_2^2}{\|\boldsymbol{\rho}_1\|\|\boldsymbol{\rho}_1 \times \boldsymbol{\rho}_2\|}, & \xi_5 &= \frac{\hat{v}_2}{\|\boldsymbol{\rho}_1\|}, \\ \xi_3 &= \frac{\hat{u}_1\hat{u}_2 + \hat{v}_1\hat{v}_2 - \hat{u}_2^2 - \hat{v}_2^2}{\|\boldsymbol{\rho}_1\|\|\boldsymbol{\rho}_1 \times \boldsymbol{\rho}_2\|}, & \xi_6 &= \frac{1}{\|\boldsymbol{\rho}_1\|}. \end{aligned} \tag{3.14} $$

Since ${\mathbf{c_1}}_A^C$ is a linear combination of $\boldsymbol{\rho_1}$ and $\boldsymbol{\rho_2}$ (Eq. (3.12)), we have

$$ \begin{bmatrix} \alpha_1 \\ \alpha_2 \end{bmatrix} = \mathbf{S}^+ \, {\mathbf{c_1}}_A^C, \tag{3.15} $$

in which $\mathbf{S}^+$ is the Moore-Penrose matrix inverse of $[\boldsymbol{\rho}_1 \;\; \boldsymbol{\rho}_2]$. Plugging Eq. (3.15) back into Eq. (3.12), we parameterize $\mathbf{t}_A^C$ with θ as

$$ \mathbf{t}_A^C = \sin(\theta) \frac{\|\boldsymbol{\rho}_1\|}{\|\boldsymbol{\rho}_1 \times \boldsymbol{\rho}_2\|} \boldsymbol{\tau_2}. \tag{3.16} $$

3.1.3.3 Reformulating Inequality Constraints

Similarly, we also reformulate the inequality constraints in Eq. (3.3b) using F_A as

$$ \|\mathbf{t}_C^A - \mathbf{q}_j^A\| \geq \epsilon_j, \;\; j = 1, 2, \tag{3.17} $$

where $\mathbf{t}_C^A$ is the unknown translation vector from F_C to F_A,

$$\mathbf{t}_C^A = \begin{bmatrix} x \\ y \\ z \end{bmatrix} = - \begin{bmatrix} (\mathbf{c_1}_A^C)^T \\ (\mathbf{c_2}_A^C)^T \\ (\mathbf{c_3}_A^C)^T \end{bmatrix} \mathbf{t}_A^C, \tag{3.18}$$

in which $\mathbf{c_1}_A^C$, $\mathbf{c_2}_A^C$ and $\mathbf{c_3}_A^C$ are respectively the first, second and third columns of $\mathbf{R}_A^C$ defined previously.

To obtain the boundary points that satisfy both the equality and inequality constraints, we use the parameterizations in Sec. 3.1.3.2 to parameterize x, y and z in $\mathbf{t}_C^A$ respectively, as follows.

First, we can parameterize x with θ using the parameterizations of $\mathbf{c_1}_A^C$ and $\mathbf{t}_A^C$ in Eq. (3.13) and Eq. (3.16),

$$x = \xi_{len} \sin(\theta)[\sin(\theta) - \frac{\hat{\mathbf{p}}_1^C \cdot \hat{\mathbf{p}}_2^C}{\|\hat{\mathbf{p}}_1^C \times \hat{\mathbf{p}}_2^C\|} \cos(\theta)], \tag{3.19}$$

in which $\cdot$ and $\times$ denote the inner product and the cross product of two vectors respectively. Let ω denote the angle between the two known vectors $\hat{\mathbf{p}}_1^C$ and $\hat{\mathbf{p}}_2^C$, which corresponds to $\angle P_1 C P_2$ as shown in Fig. 3.3. Since $\hat{\mathbf{p}}_1^C \cdot \hat{\mathbf{p}}_2^C = \|\hat{\mathbf{p}}_1^C\| \|\hat{\mathbf{p}}_2^C\| \cos(\omega)$ and $\|\hat{\mathbf{p}}_1^C \times \hat{\mathbf{p}}_2^C\| = \|\hat{\mathbf{p}}_1^C\| \|\hat{\mathbf{p}}_2^C\| \sin(\omega)$, we can simplify x as

$$x = \xi_{len} \sin(\theta)[\sin(\theta) - \cot(\omega)\cos(\theta)] = -\xi_{len} \csc(\omega) \sin(\theta) \cos(\theta + \omega). \tag{3.20}$$

Next, we parameterize y and z. Since $\|\mathbf{t}_C^A\| = \|\mathbf{t}_A^C\|$, we have

$$y^2 + z^2 = \|\mathbf{t}_A^C\|^2 - x^2 = \xi_{len}^2 \csc^2(\omega) \sin^2(\theta) \sin^2(\omega + \theta). \tag{3.21}$$

The benefit of constructing F_A shows up, again. Eq. (3.20) and Eq. (3.21) show

that both x and $y^2 + z^2$ are functions of θ. In other words, a fixed θ determines a plane in F_A with a fixed x value, and the points on that plane forms a circle with a fixed radius $\sqrt{y^2 + z^2}$, which is depicted in Fig. 3.4b. Hence, we introduce a new parameter ϕ for the angle of rotation around the x-axis of F_A, so that

$$\begin{aligned} y &= \sin(\phi)\xi_{len}\sqrt{\csc^2(\omega)\sin^2(\theta)\sin^2(\omega+\theta)}, \\ z &= \cos(\phi)\xi_{len}\sqrt{\csc^2(\omega)\sin^2(\theta)\sin^2(\omega+\theta)}. \end{aligned} \tag{3.22}$$

Finally, plugging Eq. (3.20) and Eq. (3.22) back into Eq. (3.17), we obtain two equations for the boundary

$$\sin(\theta) = \pm\sin(\omega)\epsilon_1/\xi_{len}, \tag{3.23a}$$

$$\sin(\theta+\omega) = \pm\sin(\omega)\epsilon_2/\xi_{len}, \tag{3.23b}$$

from which we can solve for eight possible pairs of $\sin(\theta)$ and $\cos(\theta)$ corresponding to eight solutions of θ.

In fact, the parameterization of $y^2 + z^2$ in Eq. (3.21) suffices our need to parameterize the boundary points. Nevertheless, the individual parameterization of y and z is useful below in Sec. 3.1.3.4.

3.1.3.4 Reformulating the Objective Function

At last, we reformulate the objective function in Eq. (3.2) using F_A as well,

$$\underset{\mathbf{R}_C^W, \mathbf{t}_C^W}{\operatorname{argmin}} \left\| \mathbf{t}_C^A - \mathbf{t}_0^A \right\|^2 \tag{3.24}$$

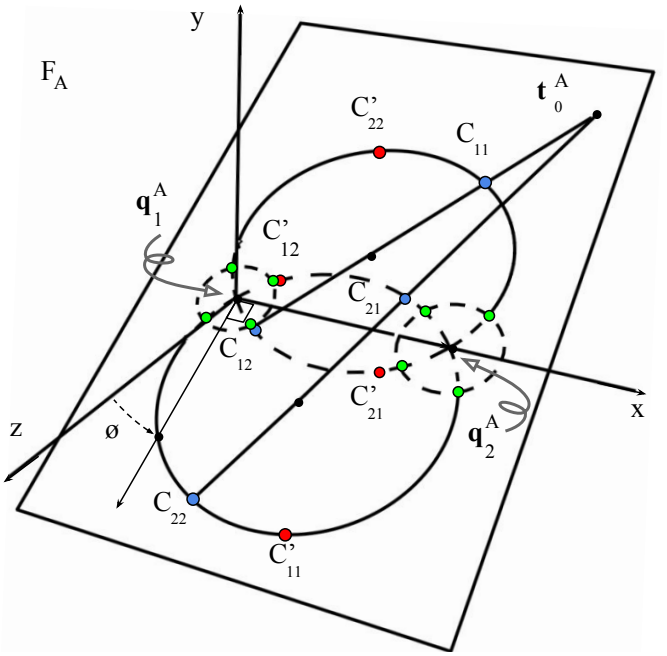

Figure 3.6: Optimal camera position candidates. $\mathbf{q}_1^A$, $\mathbf{q}_2^A$ and $\mathbf{t}_0^A$ determine a plane in F_A, which intersects with the toroidal surface and forms two solid arcs. C_{11}, C_{12}, C_{21} and C_{22} in blue are four candidates. Their symmetric points about the x-axis, C'_{11}, C'_{12}, C'_{21} and C'_{22} in red, are also candidates. The green points around $\mathbf{q}_1^A$ and $\mathbf{q}_2^A$ are eight candidates at the boundary.

in which $\mathbf{t}_0^A = \mathbf{R}_A^{W\,T}(\mathbf{t}_0^W - \mathbf{t}_A^W) = [\xi_x \;\; \xi_y \;\; \xi_z]^T$ is known. This reformulated objective function essentially means minimizing the distance from the initial camera position $\mathbf{t}_0^A$ to the toroidal surface in F_A, as shown in Fig. 3.4.

Plugging Eq. (3.20) and Eq. (3.22) into Eq. (3.24), we successfully parameterize the objective function

$$\begin{aligned} obj(\phi,\theta) =& (-\xi_{len}\csc(\omega)\sin(\theta)\cos(\theta+\omega) - \xi_x)^2 \\ &+ (\sin(\phi)\sqrt{\csc^2(\omega)\sin^2(\theta)\sin^2(\omega+\theta)} - \xi_y)^2 \\ &+ (\cos(\phi)\sqrt{\csc^2(\omega)\sin^2(\theta)\sin^2(\omega+\theta)} - \xi_z)^2. \end{aligned} \tag{3.25}$$

3.1.3.5 Minimization

To minimize *obj* with respect to ϕ and θ, we build the first-order optimality condition of Eq. (3.25), and identify all the stationary points and boundary points. First, we calculate the derivative of *obj* with respect to ϕ,

$$\frac{\partial obj}{\partial \phi} = 2\xi_{len}(\xi_z \sin(\phi) - \xi_y \cos(\phi))\sqrt{\csc^2(\omega)\sin^2(\theta)\sin^2(\theta+\omega)}. \tag{3.26}$$

Setting it to be 0, we have the following four cases,

$$\sin(\theta) = 0, \tag{3.27a}$$

$$\sin(\theta+\omega) = 0, \tag{3.27b}$$

$$\sin(\phi) = \frac{\xi_y}{\sqrt{\xi_y^2+\xi_z^2}}, \quad \cos(\phi) = \frac{\xi_z}{\sqrt{\xi_y^2+\xi_z^2}}. \tag{3.27c}$$

$$\sin(\phi) = -\frac{\xi_y}{\sqrt{\xi_y^2+\xi_z^2}}, \quad \cos(\phi) = -\frac{\xi_z}{\sqrt{\xi_y^2+\xi_z^2}}. \tag{3.27d}$$

Note that Eq. (3.27a) and Eq. (3.27b) correspond to the cases when $\mathbf{q}_1^A$ and $\mathbf{q}_2^A$ are optimal solution candidates respectively, which clearly violate the inequality constraints in Eq. (3.17). Suppose this optimization problem does not have the inequality constraints, $\mathbf{q}_1^A$ and $\mathbf{q}_2^A$ will be physically infeasible solutions. Then, other optimal solution candidates solved from Eq. (3.27c) and Eq. (3.27d) may not contain the true optimum.

Eq. (3.27c) and Eq. (3.27d) correspond to the general cases. It shows that ϕ only depends on the initial camera position $\mathbf{t}_0^A$. In fact, the angle ϕ corresponds to the plane determined by the three points, $\mathbf{t}_0^A$, $\mathbf{q}_1^A$ and $\mathbf{q}_2^A$, as shown in Fig. 3.6. Although

two solutions of ϕ can be solved from Eq. (3.27c) and Eq. (3.27d), they differ from each other by π, which essentially correspond to the same plane. Therefore, the optimal camera position sits on the plane determined by $\mathbf{t}_0^A$, $\mathbf{q}_1^A$ and $\mathbf{q}_2^A$.

Next, we substitute the two solutions of ϕ from Eq. (3.27c) and Eq. (3.27d) into the derivative of *obj* with respect to θ, and obtain the following two cases.

$$\frac{\partial obj}{\partial \theta} = \frac{\xi_{len} \csc^2(\omega)}{2E_1}(E_1E_2 + E_3E_4), \tag{3.28a}$$

$$\frac{\partial obj}{\partial \theta} = \frac{\xi_{len} \csc^2(\omega)}{2E_1}(E_1E_2 - E_3E_4), \tag{3.28b}$$

where

$$\begin{aligned} E_1 &= \sqrt{\csc^2(\omega)\sin^2(\theta)\sin^2(\theta+\omega)}, \\ E_2 &= 2\xi_x \sin(2\theta + 2\omega) + 2(\xi_{len} - \xi_x)\sin(2\theta), \\ E_3 &= \sqrt{\xi_y^2 + \xi_z^2}, \\ E_4 &= \sin(4\theta + 2\omega) - \sin(2\theta + 2\omega) - \sin(2\theta). \end{aligned} \tag{3.29}$$

E_1 can be further simplified by removing the square root with two cases,

$$E_1 = \pm \csc(\omega)\sin(\theta)\sin(\theta+\omega). \tag{3.30}$$

Setting Eq. (3.28a) and Eq. (3.28b) to be 0, we obtain four equations, among which two are duplicates, therefore, redundant. The remaining two cases can be further simplified to

$$\sin(2\theta)\xi_7 + \cos(2\theta)\xi_8 = 0, \tag{3.31a}$$

$$\sin(2\theta)\xi_9 + \cos(2\theta)\xi_{10} = 0, \tag{3.31b}$$

where ξ_k's are constant, $k = 7, 8, 9, 10$, i.e.,

$$\begin{aligned}
\xi_7 = &\ cos(2\omega)\xi_x - sin(2\omega)\sqrt{\xi_y^2 + \xi_z^2} - \xi_x + \xi_{len}, \\
\xi_8 = &\ sin(2\omega)\xi_x + cos(2\omega)\sqrt{\xi_y^2 + \xi_z^2} - \sqrt{\xi_y^2 + \xi_z^2}, \\
\xi_9 = &\ cos(2\omega)\xi_x + sin(2\omega)\sqrt{\xi_y^2 + \xi_z^2} - \xi_x + \xi_{len}, \\
\xi_{10} = &\ sin(2\omega)\xi_x - cos(2\omega)\sqrt{\xi_y^2 + \xi_z^2} + \sqrt{\xi_y^2 + \xi_z^2}.
\end{aligned} \tag{3.32}$$

Using Eq. (3.31), we can easily solve for eight possible pairs of $\sin(\theta)$ and $\cos(\theta)$ corresponding to eight general solutions of θ. Fig. 3.6 depicts the geometric meanings of the eight general solutions.

3.1.3.6 Identifying the Best Camera Position

Plugging $\sin(\phi)$, $\cos(\phi)$, $\sin(\theta)$ and $\cos(\theta)$ solved from Eq. (3.27c), Eq. (3.27d), Eq. (3.23) and Eq. (3.31) back into Eq. (3.20) and Eq. (3.22), we can get eight solutions at the boundary and eight general solutions of $\mathbf{t_C^A}$ as illustrated in Fig. 3.6. We apply three steps to identify the best camera position in F_W. First, we use the property of $\angle \mathbf{p}_1^A \mathbf{t}_C^A \mathbf{p}_2^A = \omega$ (Fig. 3.3) and the inequality constraints to eliminate the infeasible solutions. Second, among the feasible solutions, we pick $\mathbf{t}^{*A}_C$, the one with the shortest distance to $\mathbf{t}_0^A$. Finally, we compute the best camera position $\mathbf{t}^{*W}_C$ in F_W, using $\mathbf{R}_A^W$ and $\mathbf{t}_A^W$ constructed in Sec. 3.1.3.1.

3.1.3.7 Determining the Camera Orientation

The optimal orientation is uniquely determined. In Fig. 3.3, the lengths of the line segments CP_1 and CP_2 are both fixed, so the optimal camera position $\mathbf{t}^{*W}_C$ determines two more points in F_W. It is then easy and standard to retrieve the optimal camera orientation $\mathbf{R}^{*W}_C$ using these three known points [Umeyama, 1991].

3.1.3.8 Analyzing the Closed-Form Solution

At the end of this subsection, we briefly discuss the issues related to multiple optimal solutions and the change in the flying distance caused by noisy inputs.

There are three special cases with multiple optima. First, when the two object projections coincide with each other, i.e., $\omega = 0$, $\csc(\omega)$ in Eq. (3.20) is undefined. Then, x can be any arbitrary value and $y = z = 0$. This corresponds to the cases that the optimal camera positions are aligned with the two objects. Second, when the initial camera position is aligned with the two objects, i.e., $\xi_y = \xi_z = 0$, $\sin(\phi)$ and $\cos(\phi)$ in Eq. (3.27c) and Eq. (3.27d) are undefined. Then, ϕ can be any arbitrary value. The optimal camera positions form a circle. Third, when the initial camera position coincides with some point like O in Fig. 3.3, i.e., $\xi_x = \xi_{len}/2$ and $\|\mathbf{t}_A^C\| = \csc(\omega)\xi_{len}/2$. Then, solving Eq. (3.31) may yield infinitely many solutions of θ, which correspond to all the points on the solid arc in Fig. 3.3.

Using Fig. 3.6, we can intuitively see how the flying distance is affected after perturbing the inputs. There are three cases. First, if $\mathbf{t}_0^A$ stays outside the toroid before and after perturbing the inputs, the toroid's shape and size are not substantially changed, so that the flying distance does not change much either. Second, if $\mathbf{t}_0^A$ stays inside the toroid before and after perturbing, the flying distance is upper bounded by the toroid size, so that the flying distance is also stable. Third, if $\mathbf{t}_0^A$ crosses the toroid surface because of the perturbation, the flying distance is small hence stable. The next section presents the empirical results of using noisy inputs.

3.1.4 Evaluation

Though the closed-form solution is optimal, we are interested in its applicability and robustness in real photo-taking scenarios, which contain both inaccurate human inputs caused by e.g., fat-finger errors [Siek *et al.*, 2005] and imperfect robot executions.

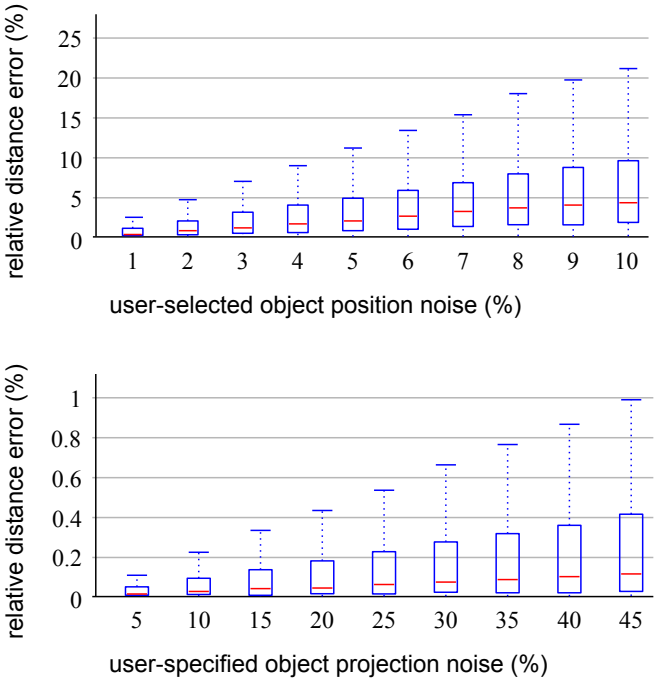

Figure 3.7: Results from synthetic datasets. The horizontal red lines indicate the medians. The boxes denote the first Q1 and third Q3 quartiles, the dashed lines extending upwards depict the statistical data extent taken to be Q3 + 1.5(Q3-Q1).

In this subsection, we first show that the resulting flying distance is robust to inaccurate user inputs. We measure the relative flying distance error using synthetic datasets. Then, we measure the quality of the resulting composition using the reprojection error with the Parrot Bebop flying camera.

3.1.4.1 Evaluation using Synthetic Data

We use synthetic datasets to show that the flying distance is robust to inaccurate user inputs.

First, we generate ground truth data. We randomly generate 10,000 different sets of inputs. Each set consists of an initial camera position $\mathbf{t}_0^W$, two object centroids $\mathbf{q}_1^W$ and $\mathbf{q}_2^W$, two collision-free distances ϵ_1 and ϵ_2, and two object projections $\mathbf{p}_1^I$

and $\mathbf{p}_2^I$ on the image plane. The image size is 1920×1080. $\mathbf{t}_0^W$, $\mathbf{q}_1^W$ and $\mathbf{q}_2^W$ are uniformly drawn from a unit cube $[0, 1]^3$. ϵ_1 and ϵ_2 are uniformly generated so that $\epsilon_1 + \epsilon_2 \leq \|\mathbf{q}_1^W - \mathbf{q}_2^W\|$. $\mathbf{p}_1^I$ and $\mathbf{p}_2^I$ are uniformly drawn within the image size.

Then, we consider two types of noise introduced by inaccurate user inputs.

Noisy User-Selected Object Positions During object selection, the object positions may be inaccurately estimated. We corrupt $\mathbf{q}_1^W$ and $\mathbf{q}_2^W$ with noise that follows a uniform distribution around the original object centroids. The noise ranges from 1% to 10% of their original relative distances in 3D.

Noisy User-Specified Object Projections During direct manipulation, the object projections may not be specified accurately as in one's mind. We corrupt $\mathbf{p}_1^I$ and $\mathbf{p}_2^I$ with noise that follows a uniform distribution around the original object projections. The noise ranges from 5% to 45% of their original relative distances on the image to ensure non-overlapping sampling regions.

Measurement We measure the relative flying distance error denoted as

$$Error_{dist}(\%) = \frac{|d_{noisefree} - d_{noisy}|}{\|\mathbf{q}_1^W - \mathbf{q}_2^W\|}, \tag{3.33}$$

in which $d_{noisefree} = \|\mathbf{t}_0^W - \mathbf{t}_{noisefree_C}^W\|$ is the distance from the initial camera position $\mathbf{t}_0^W$ to the optimized final position $\mathbf{t}_{noisefree_C}^W$ based on noise-free user inputs, $d_{noisy} = \|\mathbf{t}_0^W - \mathbf{t}_{noisy_C}^W\|$ is the distance from $\mathbf{t}_0^W$ to the optimized position $\mathbf{t}_{noisy_C}^W$ based on corrupted user inputs, and $\|\mathbf{q}_1^W - \mathbf{q}_2^W\|$ indicates the scale of the environment.

Fig. 3.7 shows that the flying distance solved using our method is robust to very noisy user inputs in both cases.

3.1.4.2 Evaluation with Parrot Bebop

To show our closed-form solution is applicable in real flying camera photography, we evaluate it on the Parrot Bebop drone whose camera resolution is 1280×720. Please refer to Sec. 5.1 for a detailed system hardware and software setup.

Robot Trajectory Execution Here, we highlight the necessary system components to reach the computed POV with the Parrot Bebop drone.

The 6 DoFs camera pose is estimated using ORB-SLAM [Mur-Artal *et al.*, 2015] without other external sensors. However, the drone driver [AutonomyLab, 2018] only supports 5 DoFs camera control. We enable the 6th DoF by rotating the image plane, so that the effective image area becomes a circular area at the center of the image, as in Fig. 3.9. Due to the hardware constraint, the pan-tilt range is also limited, so that some viewpoints are not achievable.

The camera flying trajectory is modeled as a straight line connecting the initial camera position to the goal position, by assuming the environment to be free of major obstruction for flying. The camera orientation is computed based on its position at that moment, in order to minimize the composition error Eq. (3.1) at all times.

To execute the flying trajectory, each DoF of the camera is controlled by an independent PID controller. The control gains are fine-tuned by assuming that the SLAM map is in the metric unit. To resolve the scale ambiguity of the SLAM map, we adopt a scale estimation method using the onboard ultrasonic altitude measurement [Engel *et al.*, 2014b].

In practice, the goal camera viewpoint can never be achieved. A viewpoint is considered as *successful*, if it satisfies all the following conditions. The camera position error is below 0.5 meter. The orientation error is below 1 degree. All control signals at that moment are below certain thresholds as well.

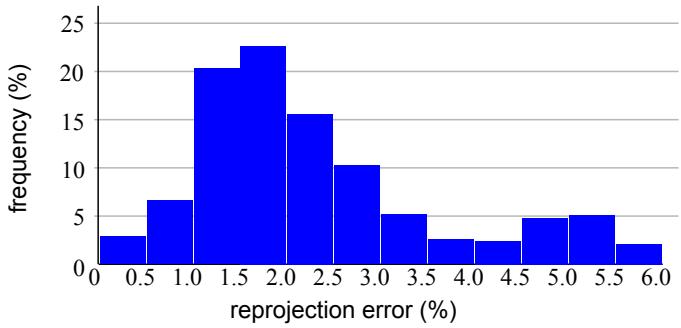

Figure 3.8: Results from real robot experiments.

Data Collection The experiments are conducted in an indoor environment of size $8m \times 6m \times 2.5m$. We use two distinctive colored balls of diameter $10cm$ to represent two objects of interest. We place the two balls at fixed locations in the center area of the room. Their distance is 1.5 meter from each other.

We collect data from 50 trials. After building a SLAM map, we place the camera at the locations of the two balls to record their positions $\mathbf{q}_1^W$ and $\mathbf{q}_2^W$ in the SLAM map. Since the objects in real photo-taking scenarios have various shapes, we are not interested in the accuracy of object centroid estimation. We set the collision-free distances ϵ_1 and ϵ_2 to be $0.5m$ and $0.8m$ respectively.

For each trial, we randomly generate $\mathbf{t}_0^W$ within the environment. We also randomly generate $\mathbf{p}_1^I$ and $\mathbf{p}_2^I$ that are uniformly drawn from the circular area of diameter 700 pixels at the center of the image. We collect 30 frames at the successful viewpoints from each trial. We reject the unreachable viewpoints that are outside the environment or beyond the camera pan-tilt range limits.

Measurement We measure the composition error using the reprojection error on each collected frame. For each frame, we exact the centroid pixel $\mathbf{p}_{exacted_j}^I$ for each ball j, and measure the distance to its corresponding desired composition, $e_j = \|\mathbf{p}_{exacted_j}^I - \mathbf{p}_j^I\|$. Hence, the reprojection error of a frame with respect to the im-

age size is $Error_{reproj}(\%) = (e_1 + e_2)/(2 \times 720)$.

The histogram in Fig. 3.8 shows the distribution of reprojection errors. Overall, the reprojection errors are relatively small, under very challenging conditions, including imperfect controls, SLAM system errors, etc.

3.1.4.3 Viewpoint Changing Process

We illustrate the viewpoint changing process while composing two objects using a concrete scenario. As shown in Fig. 3.9, the scenario starts from a high-angle viewpoint. The two main parts of the sculpture are selected as the objects of interest. We build the SLAM map, and record the estimated object positions. We manually specify the desired compositions for the objects in order to emulate the end points of direct manipulation gestures.

The viewpoint changes in two steps. First, it quickly changes the orientation to compose one object, since changing orientation is much faster than flying. Gradually, the other object converges to the desired composition while the camera is moving towards the goal. This phenomenon is caused by the fact that the orientation is recomputed based on the camera position at that time in order to minimize the reprojection error.

3.1.5 Discussion

The evaluation results show that our closed-form solution to the formulated optimization problem is applicable to real flying robot systems. Our problem focuses on a subset of aspects that are important to flying camera photography, including minimizing the flying distance, and avoiding collisions with objects of interest. We believe the formation could be generalized to include other aspects as well, such as stabilizing the frame by removing one DoF from rotation, or collision-free flying by

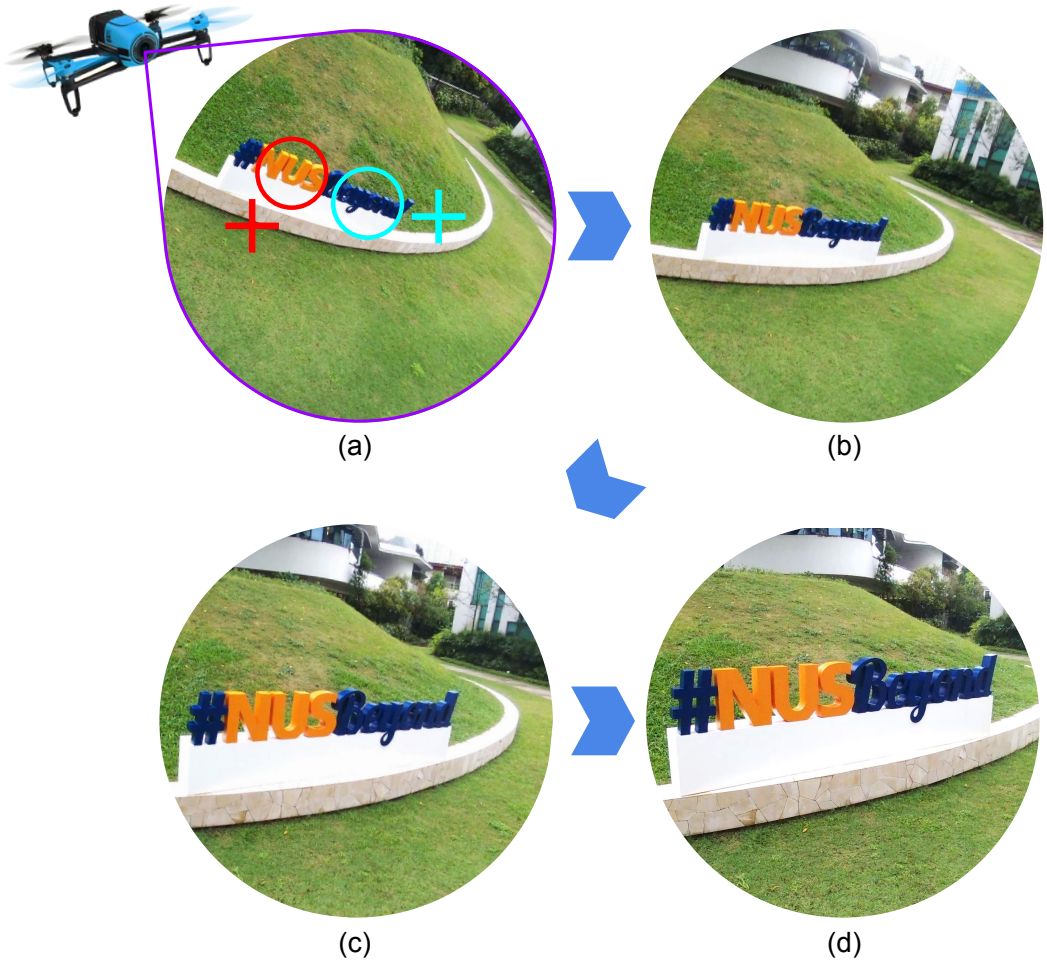

Figure 3.9: The viewpoint changing process. (a) In the initial viewpoint, each colored circle annotates an object that is composed to the position indicated by the same colored cross. (b) The viewpoint rotates to compose one object first. (c) The viewpoint moves so that the other object gradually converges to the desired composition. (d) The final viewpoint.

adding constraints for obstacles in the environments.

In addition to the two objects composition problem studied in this section, we describe a method for three or more objects in the next section.

3.2 Three or More Objects Composition

To compose multiple objects, we propose a sample-based method that solves the problem with an approximate POV, which is easy to implement, and can be applied to solve two objects composition problem as well.

The idea is to sample multiple candidate POVs and pick the best one. However, the space of POVs is very large. To achieve real-time performance, we reduce the sampling space by decoupling the camera position and the camera orientation. We only sample camera positions, and at each sampled camera position we find an approximately optimal orientation. The details are described below.

First, the method samples many camera positions as candidates around the current POV. Those camera positions are sampled unevenly: it is denser near the current POV and sparser further away (with an upper bound). This sampling strategy is to increase the chance of finding good nearby POVs in order to minimize the potential flying distance. Second, the candidate orientation at each candidate position is estimated by averaging multiple orientations. Each is the optimal orientation at that candidate position for one object. At last, the candidate POV with the minimum composition error is returned.

The POV found by this sampled-based method is an approximate solution that may not be globally optimal. However, since the dragging gestures are imprecise touch inputs after all, it is unnecessary to over-interpret those gestures very accurately.

3.3 Summary

We investigated the underlying POV search problem for composing multiple objects of interest. Sec. 3.1 solved the P2P problem for composing two objects of interest. To the best of our knowledge, it is the first study that determines the camera parameters given an under-constrained system. By incorporating the user's composition requirements and minimizing the camera's flying distance, we formed a constrained nonlinear optimization problem, solved it in closed form, and evaluated the applicability in real flying camera systems. Sec. 3.2 proposed a general sample-based method to solve the multiple objects composition problem. In system evaluation (Chap. 6), we implement this method to evaluate the explore-and-compose paradigm proposed in Sec. 2.1.2.

In this chapter, the proposed methods assume that the intended POV can be achieved safely without colliding with obstacles. Next, we study the depth perception problem for collision avoidance with a monocular camera in the following chapter.

Chapter 4

Depth Perception for Collision Avoidance

XPose promotes direct interactions with images by keeping the tedium of low-level drone control away from the user. Autonomously avoiding collision with obstacles while reaching user intended POVs is, therefore, an important system capability. Our envisioned flying camera in the future is a portable drone fitted with a light-weight monocular camera with little power consumption (Fig. 4.1). This chapter is dedicated to investigating the collision avoidance problem using a monocular camera.

Using monocular cameras for collision avoidance and obstacle perception remains

(a) (b) (c)

Figure 4.1: Portable flying cameras. (a) A palm-sized flying camera [Cheerson, 2018]. (b) A phone-sized flying camera [AirSelfie, 2018]. (c) A wearable flying camera [Flynixie, 2018].

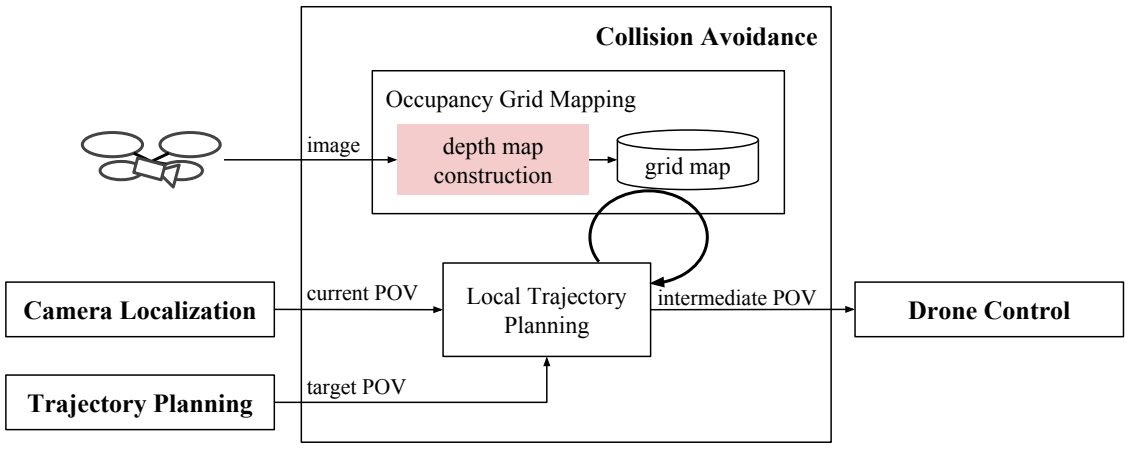

Figure 4.2: Information flow for collision avoidance component. This chapter focuses on the depth map construction problem highlighted in red.

an area of active research in robotics and computer vision. One main approach is to learn a policy that maps from images to actions end-to-end using training data. The learned policies have enabled flying cameras to navigate in the forest [Ross *et al.*, 2013] and indoor environments [Sadeghi and Levine, 2017]. However, such end-to-end approach is data-hungry and suffers from the problem of generalizability in new environments.

Compared with data collection for the end-to-end approach, it is much easier to acquire depth information for obstacle perception using, for example, Structure-from-Motion (SfM) [Schonberger and Frahm, 2016], Multi-View Stereo (MVS) [Furukawa *et al.*, 2010] and RGB-D image datasets [Saxena *et al.*, 2009; Silberman and Fergus, 2011; Geiger *et al.*, 2013; Li and Snavely, 2018]. This leads to a modular approach to the collision avoidance problem by solving two sub-problems: mapping and planning.

Fig. 4.2 illustrates our modular design of the collision avoidance component. For the planning module, there are many standard motion planning algorithms, such as potential field [Khatib, 1985], A*, RRT* [Karaman and Frazzoli, 2010], etc. The major challenge lies in the mapping module that constructs an accurate depth map

using images captured from a monocular camera in real time, which is the main focus of this chapter.

4.1 Depth Map Construction

A monocular camera can perceive depth in real time through geometry-based approach and data-driven approach. On the one hand, the geometry-based approach usually provides robust depth estimations of visual features sparsely extracted from the image. On the other hand, the data-driven approach usually estimates dense depth maps. However, their depth estimations are prone to errors, which are not as accurate as the depth estimations based on geometric models.

Our key idea is to join the strengths from both geometry-based and data-driven approaches. Intuitively, we rely on the accurate depth map from geometric models to refine the error-prone dense depth map. In other words, we use the dense depth map as a prior to upsample the accurate sparse depth map.

In this section, we first review the geometry-based and data-driven approaches (Sec. 4.1.1). Next, we give a formal definition to our depth map construction problem (Sec. 4.1.2). Then, we present our depth map construction pipeline (Sec. 4.1.3). Finally, we conduct experiments on real world image datasets for evaluation (Sec. 4.1.4).

4.1.1 Related Work

4.1.1.1 Geometry-based Approach

Geometry-based approach to monocular depth perception includes feature-based methods and direct methods. Feature-based methods [Klein and Murray, 2007; Mur-Artal *et al.*, 2015] first extract a set of corner features from the image. Then, the scene geometry is computed only based on the corners, resulting in a very sparse depth

map. By contrast, direct methods do not extract features. They optimize the scene geometry based on the image intensity changes over consecutive frames. In addition to corners, edges from the image may also have robust depth estimations, resulting a semi-dense depth map [Forster *et al.*, 2014; Engel *et al.*, 2014a]. Dense mapping with direct methods has also been studied [Newcombe *et al.*, 2011], but in small-scale environments.

A recent method, FLaME [Nicholas Greene and Roy, 2017], combines feature-based and direct methods to construct dense 3D depth maps for flying robot navigation. The idea is to extract point features uniformly from the image and estimate their depths using direct search along the epipolar lines. Finally, the sparse depth map is *densified* by smoothly propagating the sparse information out using a Delaunay triangulation on the image plane. This method was implemented on a flying drone for collision avoidance. However, the method relies on very accurate camera poses and high-quality image streams, which cannot be reliably acquired for low-cost commercial drones, such as Parrot Bebop drones. In our system implementation, we use ORB-SLAM [Mur-Artal *et al.*, 2015] to construct a sparse depth map due to its robustness in practice. Inspired by FLaME, we perform Delaunay triangulation to propagate the sparse information.

4.1.1.2 Data-driven Approach

Monocular depth estimation can also be data-driven, i.e., learned from training data. There is a large body of work that focuses on supervised learning methods [Liu *et al.*, 2014; Eigen and Fergus, 2015; Li *et al.*, 2015; Liu *et al.*, 2015; Laina *et al.*, 2016; Xu *et al.*, 2017], which learns a mapping from monocular images to their depth maps. By contrast, unsupervised learning methods do not need ground truth depth images [Godard *et al.*, 2017; Zhou *et al.*, 2017]. Instead, stereo images are used. Deep neural networks are trained to synthesis disparity maps for reconstructing stereo images.

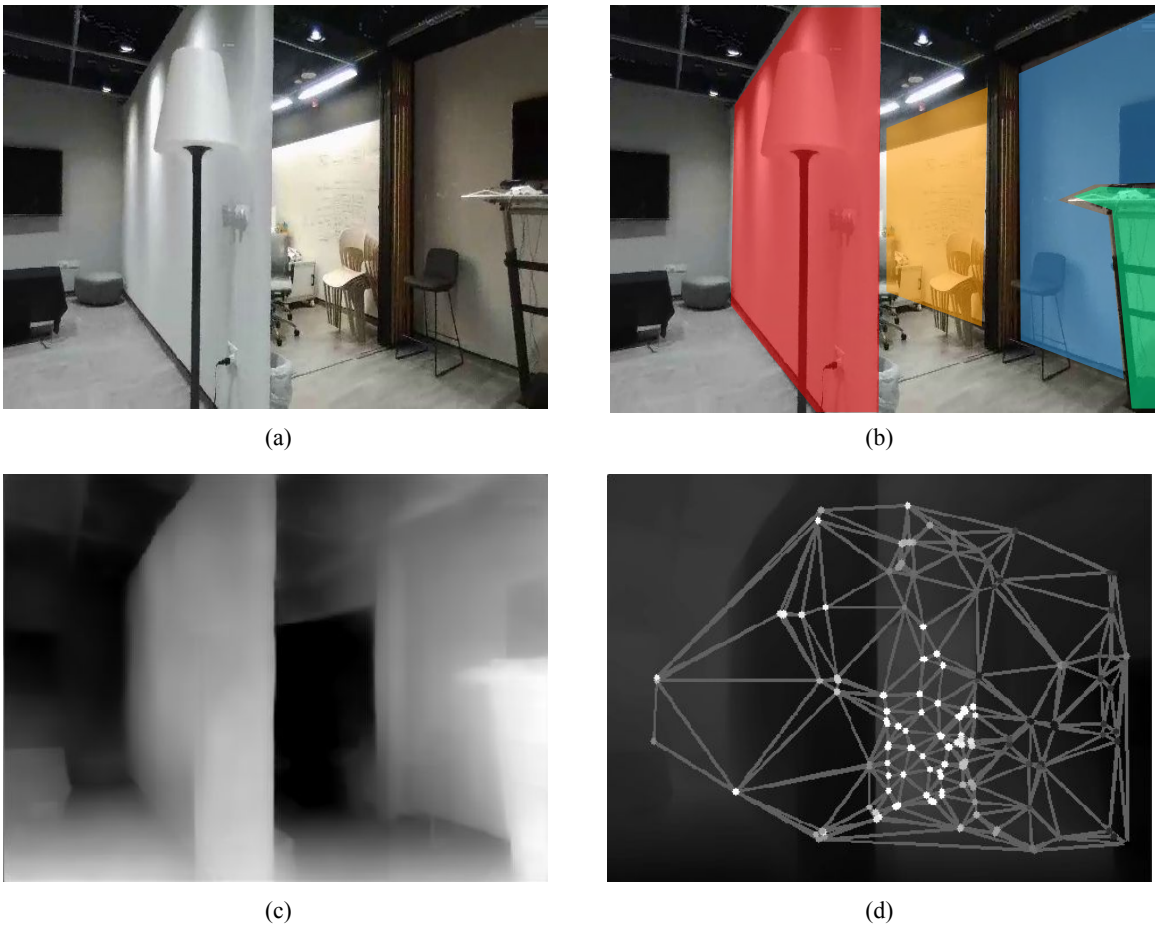

(a) (b) (c) (d)

Figure 4.3: Monocular depth perception. (a) Original RGB image. (b) Regions of interest masked out from the image: a texture-less wall (red), a wall under different lighting conditions (orange and blue), and a table (green). (c) Gray-scale image encoding the dense depth map predicted by a deep neural network pre-trained on MegaDepth. A darker color indicates a larger depth. Note that the depth estimation is prone to errors. The edge of the wall (red) shall be closer than the table (green). The wall under different lighting conditions (orange and blue) shall have a smooth depth transition. (d) Delaunay triangulation of ORB-SLAM features. Note that the features are sparse and distributed unevenly: the texture-less wall (red) occupies a large region but has very few features. The grey-scale colors on the features encode the sparse scale map $\hat{S}_F$ (Eq. (4.4)). A darker color indicates a larger scale.

Then, it is trivial to recover depth maps from the disparity maps.

One major issue for the data-driven approach is the acquisition of high-quality training data. Most datasets of depth images [Saxena *et al.*, 2009; Geiger *et al.*, 2013; Silberman and Fergus, 2011] and stereo image pairs [Geiger *et al.*, 2013; Schöps *et al.*, 2017] are either small or collected in specific scenarios, which potentially affect the generalizability of the methods.

MegaDepth [Li and Snavely, 2018] proposed to use multi-view internet photo collections, a virtually unlimited data source, to generate training data. First, geometric methods (Structure-from-Motion and Multi-View Stereo) are applied on the internet photo collections to construct 3D models, hence, provide depth maps. Then, a semantic filtering is used to identify images with large transient objects in their foreground, such as selfies. These "selfie" images are dedicated to training the (ordinal) depths of transient objects that are difficult to obtain during geometric construction. The "non-selfie" images are used to train the (Euclidean) depths directly. Training on the resulting datasets is able to generalize very well to other datasets and new environments. Therefore, we use a deep neural network pre-trained on MegaDepth to provide a base dense depth map in our system implementation, despite it is prone to making errors (Fig. 4.3c).

We re-scale the base depth map to ensure its scale is consistent with the sparse depth map. This is conceptually equivalent to combining a handful set of base depth maps with different scales into a final depth map. Similar to our usage of base depth maps, CodeSlam [Bloesch *et al.*, 2018] and BA-Net [Tang and Tan, 2018] also use neural networks to recover many base depth maps and then recover the final depth map as a linear combination of these bases.

In the following subsections, we formally define our problem setup and show the depth map construction pipeline.

4.1.2 Problem Formulation

Let P be the set of all image pixels. Our goal is to construct an accurate and dense depth map,

$$\hat{D}_P = \{\hat{d}_p | p \in P\}. \tag{4.1}$$

We are given two depth maps as the sources of input. First, ORB-SLAM estimates an accurate but sparse depth map,

$$\hat{D}_F^{GEO} = \{\hat{d}_f^{GEO} | f \in F \subset P\}, \tag{4.2}$$

where F is sparse. Second, MegaDepth offers a dense but error-prone depth map,

$$\hat{D}_P^{LRN} = \{\hat{d}_p^{LRN} | p \in P\}. \tag{4.3}$$

4.1.3 Depth Map Construction Pipeline

We first analyze the problem and give an overview of our depth map construction pipeline, then describe each step in detail.

Since monocular depth estimations are inherently scale ambiguous, both ORB-SLAM and MegaDepth methods have different conventions to determine scales: the scales of depth maps produced by ORB-SLAM are consistent over all frames, whereas the scales of depth maps learned from MegaDepth are different for the frames. A consistent scale is preferred in order to aggregate individual depth map into an occupancy grid map (Fig. 4.2).

Therefore, we have to estimate the scale between the sparse and dense depth maps. To this end, our depth map construction consists of three main steps. First, we use the sparse depth map to construct a sparse scale map. Then, we upsample the sparse scale map. Finally, we perform a pixel-wise scaling on the dense depth map to

obtain our desired dense depth map.

4.1.3.1 Sparse Scale Map Construction

With a sparse depth map $\hat{D}_F^{GEO}$ and a dense depth map $\hat{D}_F^{LRN}$, we first compute a sparse scale map $\hat{S}_F$,

$$\hat{S}_F = \{\hat{s}_f = \frac{\hat{d}_f^{GEO}}{\hat{d}_f^{LRN}} | f \in F \subset P\}. \tag{4.4}$$

In practice, $\hat{D}_F^{GEO}$ contains outliers, so that $\hat{S}_F$ is contaminated with outliers as well. In the ideal case, however, all $\hat{s}_f$'s shall be the same. This is a useful prior to prune those outliers. It is convenient to use the interquartile range (IQR) rule to identify outliers that are far away from the median.

However, since the sparse set of features is not uniformly distributed in general (Fig. 4.3d), features in the dense region dominate the overall distribution. Hence, instead of applying the IQR rule globally on the whole set of $\hat{S}_F$, we apply it on a local neighborhood set $Neighbors(f)$ of each feature f.

There are two popular choices of neighborhood sets: features within some fixed distance and k-nearest-neighbors. However, they are also not suitable when the features are not uniformly distributed: neighbors from the dense region dominate again.

We define a neighborhood set based on the Delaunay triangulation of F. More specifically, $Neighbors(f)$ is defined as the set of vertices such that they belong to the distance-1 or distance-2 neighborhood of vertex f on the triangulation. Our definition of neighborhood ensures the neighbors are distributed around vertex f. Fig. 4.3d is an example of the sparse scale map after outliers removed.

4.1.3.2 Dense Scale Map Construction

For each image pixel $p \in P \backslash F$, we find a set of nearby vertices $\{p_i\}$ that enclose p in the triangulation as shown in Fig. 4.5. Its estimated scale $\hat{s}_p$ is a weighted sum of

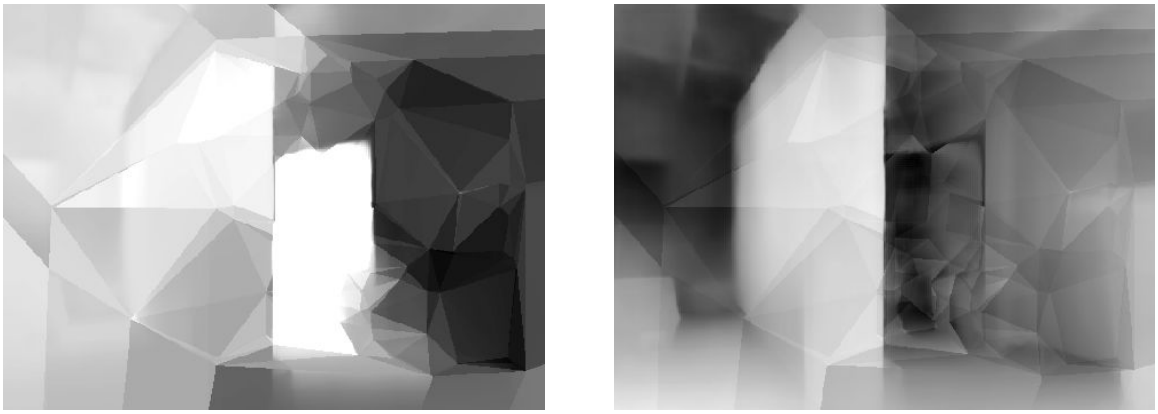

(a) (b)

Figure 4.4: Monocular dense depth map construction. Refer to Fig. 4.3. (a) Gray-scale image encoding the dense scale map. A darker color indicates a larger scale. Note that the scale map tends to preserve the boundaries between semantic objects. (b) Gray-scale image encoding the dense depth map. A darker color indicates a larger depth. Note that the depths of the regions marked in Fig. 4.3b are corrected.

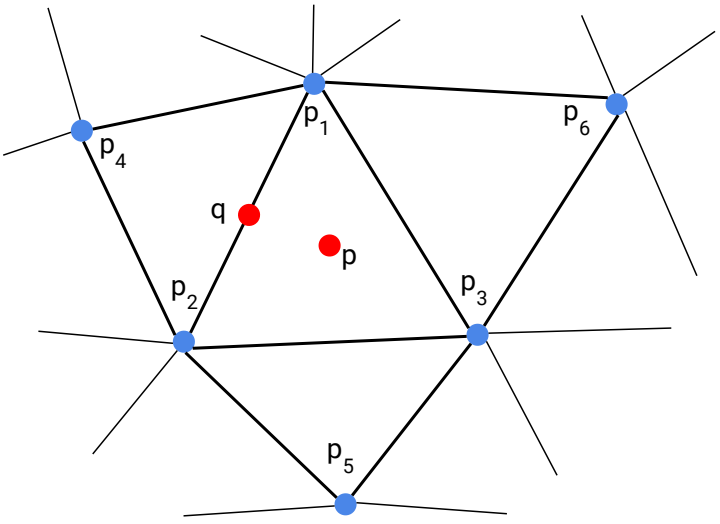

Figure 4.5: Nearby vertices that enclose a pixel. For a pixel p within a triangle, we use 6 vertices $\{p_1, p_2, ..., p_6\}$ to compute $\hat{s}_p$. For a pixel q on an edge, we use 4 vertices $\{p_1, p_2, p_4, p_4\}$.

the scales of these nearby vertices, i.e.,

$$\hat{s}_p = \frac{\sum_i w_{p_i} \hat{s}_{p_i}}{\sum_i w_{p_i}}, \tag{4.5}$$

where

$$w_{p_i} = exp(-\frac{|\hat{d}_p^{LRN} - \hat{d}_{p_i}^{LRN}|^2}{\sigma_{LRN}^2}), \quad \forall i. \tag{4.6}$$

The weight w_{p_i} is designed to consider object semantic information encoded in the dense depth map. Since object semantics are used to guide the training in MegaDepth dataset, pixels belonging to the same semantic object tend to have similar depths in the predicted depth map. As a result, Fig. 4.4a is an example of reconstructed dense scale map.

4.1.3.3 Dense Depth Map Construction

With Eq. (4.4) and (4.5), we obtain a dense scale map $\hat{S}_P = \{\hat{s}_p | p \in P\}$. Finally, we use it to scale the dense depth map $\hat{D}_P^{LRN}$, and have our desired dense depth map,

$$\hat{D}_P = \{\hat{d}_p = \hat{s}_p \hat{d}_p^{LRN} | p \in P\}. \tag{4.7}$$

4.1.4 Evaluation

In this subsection, we evaluate our dense map reconstruction method on two real world image datasets: Make3D [Saxena *et al.*, 2009] and Kitti [Geiger *et al.*, 2013]. Following previous works [Li and Snavely, 2018], we adopt three evaluation metrics to quantitatively assess its performance: (1) rooted mean square error (RMS): $\sqrt{\frac{1}{N}\sum_i (\hat{d}_i - d_i^*)^2}$, (2) mean relative error (AbsRel): $\frac{1}{N}\sum_i \frac{|\hat{d}_i - d_i^*|}{d_i^*}$, and (3) mean log10 error (LOG10): $\frac{1}{N}\sum_i |\log_{10} \hat{d}_i - \log_{10} d_i^*|$, in which N is the total number of ground-truth depths, d_i^* is the ground-truth depth at pixel i, and $\hat{d}_i$ is the estimated depth

using our method.

To test on the datasets, we use the neural network, trained on MegaDepth only, to produce the input dense depth maps. In addition, we synthesis the input sparse depth maps as follows. We randomly sample $\kappa\%$ of ground truth depths to form sparse depth maps, $\kappa = 1, 2, 3, 4, 5$. To emulate outliers, we randomly sample 1% from the sparsely sampled depths, and multiply them by a random number between 3 to 10. For the rest 99% samples, we corrupted them with noise, to emulate noisy measurements.

Make3D To test on Make3D, we follow the protocol of prior work [Liu *et al.*, 2015] to remove ground truth depths larger than 70m (since Make3D data is unreliable at large distances). Table 4.1 summarizes the results. Results from other algorithms are reported in [Li and Snavely, 2018]. The bottom block of Table 4.1 shows that our method outperforms prior state-of-the-art results. As expected, all errors decrease monotonically when we increase κ.

KITTI Next, we evaluate our method on the KITTI test set based on the split of [Eigen *et al.*, 2014]. Table 4.2 summarizes the results. Similar to the case in Make3D, our method achieves the state-of-the-art accuracy, and all errors decrease monotonically when we increase κ.

4.1.5 Discussion

The evaluation results show that our method is able to reconstruct dense and accurate depth map for obstacle perception. Not surprisingly, increasing the number of accurate input depths improves the overall accuracy.

While our method for depth perception is shown to be effective, it is not ready to be used in an overall system evaluation for photo-taking in the current stage, due

Training set	Method	RMS	AbsRel	LOG10
Make3D	[Karsch *et al.*, 2014]	9.2	0.355	0.127
	[Liu *et al.*, 2014]	9.49	0.355	0.137
	[Liu *et al.*, 2015]	8.6	0.314	0.119
	[Li *et al.*, 2015]	7.19	0.278	0.092
	[Laina *et al.*, 2016]	4.45	<u>0.176</u>	0.072
	[Xu *et al.*, 2017]	4.38	0.184	<u>0.065</u>
MegaDepth	[Li and Snavely, 2018]	5.49	0.298	0.115
MegaDepth+Make3D		<u>4.26</u>	<u>0.176</u>	0.069
MegaDepth+1%	Ours	4.17	0.155	0.062
MegaDepth+2%		3.68	0.127	0.050
MegaDepth+3%		3.42	0.112	0.044
MegaDepth+4%		3.24	0.103	0.041
MegaDepth+5%		3.12	0.097	0.038

Table 4.1: Results on Make3D dataset. The first column shows the training datasets. For our method, $\kappa\%$ metric observations are used to synthesis the sparse depth maps. Lower is better for all error metrics. The underlined numbers are prior state-of-the-art results.

Training set	Method	RMS	AbsRel	LOG10
KITTI	[Eigen *et al.*, 2014]	6.31	0.203	0.081
	[Liu *et al.*, 2016]	6.52	0.202	0.080
	[Zhou *et al.*, 2017]	6.86	0.208	0.082
	[Godard *et al.*, 2017]	5.93	0.148	0.060
MegaDepth	[Li and Snavely, 2018]	6.87	0.282	0.108
MegaDepth+KITTI		<u>5.90</u>	<u>0.141</u>	<u>0.057</u>
MegaDepth+1%	Ours	3.22	0.085	0.026
MegaDepth+2%		2.82	0.078	0.022
MegaDepth+3%		2.61	0.075	0.019
MegaDepth+4%		2.46	0.073	0.018
MegaDepth+5%		2.36	0.072	0.012

Table 4.2: Results on KITTI dataset. The first column shows the training datasets. For our method, $\kappa\%$ metric observations are used to synthesis the sparse depth maps. Lower is better for all error metrics. The underlined numbers are prior state-of-the-art results.

to a major hardware constraint: the Parrot Bebop's forward-facing camera has a very limited viewing angle. The flying camera has to fly around slowly to build the occupancy grid map before the system plans for a collision-free path, which adversely affects the seamless photo-taking experience. This limitation can be overcome by using a wide angle camera, such as an omnidirectional camera. Existing SLAM systems for omnidirectional cameras [Caruso *et al.*, 2015] can be used to estimate the sparse depth maps. In addition, the MegaDepth dataset requires modification to train a neural network for the omnidirectional cameras as well.

4.2 Summary

We are pursuing a modular approach to the collision avoidance problem. In this chapter, we focused on the mapping module that constructs an accurate depth map. To realize the collision avoidance capability, we integrate our depth map construction pipeline into the collision avoidance component as shown in Fig. 4.2. The integration details are described in the next system implementation chapter.

Chapter 5

System Implementation

We show the system implementation details in this chapter. First, we provide system hardware and software setup (Sec. 5.1). Then, we describe the system components (Sec. 5.2) implementing the system functions for our explore-and-compose paradigm (Sec. 2.2).

5.1 System Hardware and Software Setup

5.1.1 Hardware

Our system uses a Parrot Bebop drone with a built-in forward-facing camera. The user's mobile device is an ASUS Google Nexus 7 (2012) tablet with a 7.0" multi-touch display, running Android version 5.1. Both the drone and the tablet are connected via Wi-Fi to a laptop PC with an Intel Core i7 processor and a GTX 1060 GPU.

5.1.2 Software

We use an open-source drone driver, Bebop Autonomy [AutonomyLab, 2018], to communicate with the Bebop at 30 Hz. The Bebop runs low-level controllers onboard.

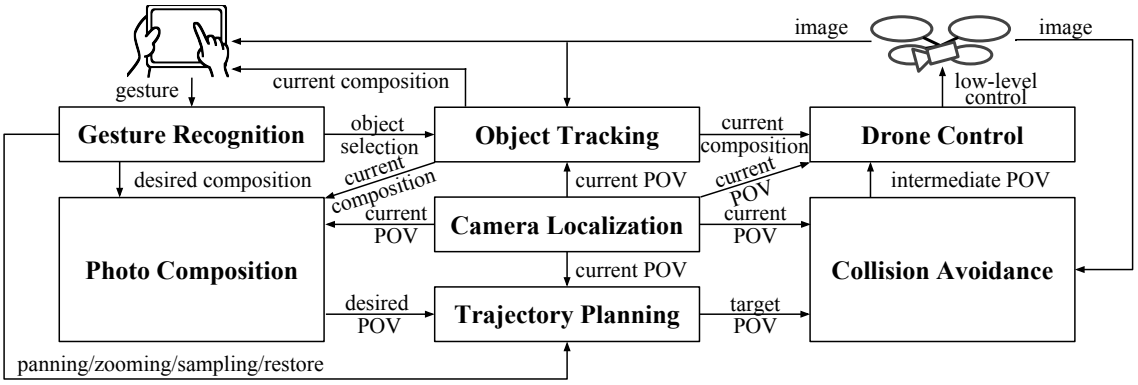

Figure 5.1: Overview of the system architecture.

The tablet runs Rosjava and detects gestures using Android's gesture detection library. The PC handles all other computations. It also hosts the Robot Operating System framework, which is used to establish communication among the drone, the tablet, and the laptop PC.

5.2 System Components

Fig. 5.1 presents an overview of the system architecture tightly integrating the seven main system components. Information flow among the system components is annotated. Next, we describe each system component in detail.

5.2.1 Gesture Recognition

XPose uses Android's standard gesture detection library to detect three main types of gestures on the touchscreen (Fig. 5.2): single-finger swiping gestures, multi-finger gestures, and button clicking gestures. Single-finger gestures mainly consists of encircling gesture for object selection (Fig. 1.3a) and dragging gesture for object composition (Fig. 1.3g). Multi-finger gestures refer to panning/zooming gestures as introduced in Fig. 2.1. Button clicking gestures enable various main system functions such as POV

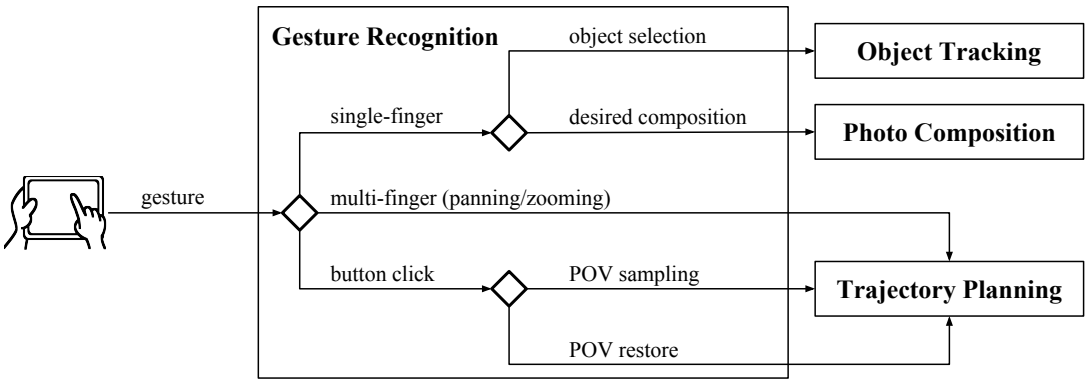

Figure 5.2: Information flow for gesture recognition component.

sampling (Fig. 1.3b) and POV restore (Fig. 1.3f).

5.2.2 Camera Localization

Unlike hand-held cameras, our flying camera explores POVs globally. It must have a greater awareness of the surrounding environment, and localization becomes a crucial issue. XPose uses a state-of-the-art monocular visual SLAM algorithm, ORB-SLAM [Mur-Artal *et al.*, 2015], to build a SLAM map and localize the camera with respect to a fixed world coordinate. Localization provides real-time camera POVs.

5.2.3 Object Tracking

For robust object selection and tracking, we exploit ORB-SLAM and use the sparse points produced by the algorithm to represent objects. ORB-SLAM is a feature-based visual SLAM system. It provides 2D-to-3D point correspondence: each 2D feature point exacted from the image is associated with a 3D map point in the SLAM map.

For object selection, the 2D feature points encircled by the user's stroke and their corresponding 3D map points are used to represent an object. All selected objects are stored and used to realize object tracking in real time (Fig. 5.3).

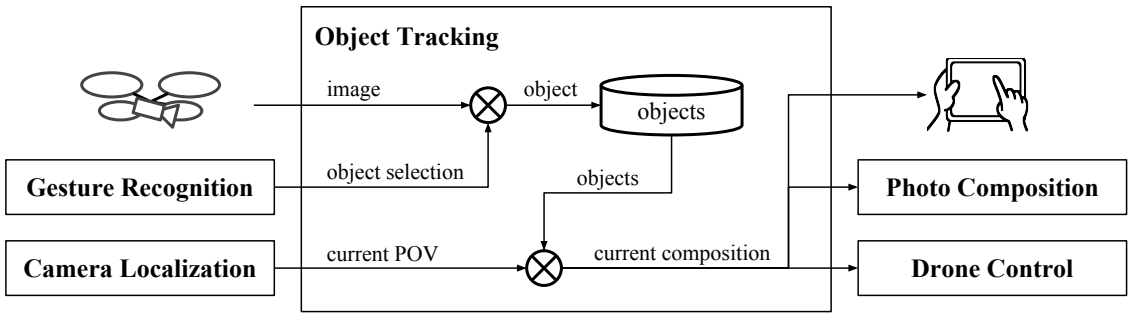

Figure 5.3: Information flow for object tracking component.

For object tracking, we need to display a bounding box around each selected object on the image as a visual cue. First, for simplicity, we compute the center of the bounding box as the 2D projection of the centroid of each object. An object centroid is estimated as a weighted average of its 3D map points. We assume the points closer to the center of the selected region are more important and therefore have higher weights. Then, the bounding box size is continuously estimated by computing the distance from the camera to the object centroid.

The center of the bounding box is a simplified representation of an object's composition location. For simplicity, we directly use the center of the bounding box as the actual composition location, and the ending point of the direct manipulation gesture as the desired composition location. Following the definition in Eq. (3.1), the composition error is simply the distance between the two points on the image plane.

This object-tracking implementation, based on ORB-SLAM, is robust against many practical issues common to drone-mounted cameras, such as temporary frame drops, occlusions, camera exposure changes, etc. Unlike (semi-)dense SLAM algorithms (e.g., [Concha and Civera, 2015; Engel *et al.*, 2014a; Pizzoli *et al.*, 2014]), ORB-SLAM tracks a relatively sparse set of features, but it is sufficient for object tracking in our experiment, provided, of course, enough feature points are extracted from the objects of interest.

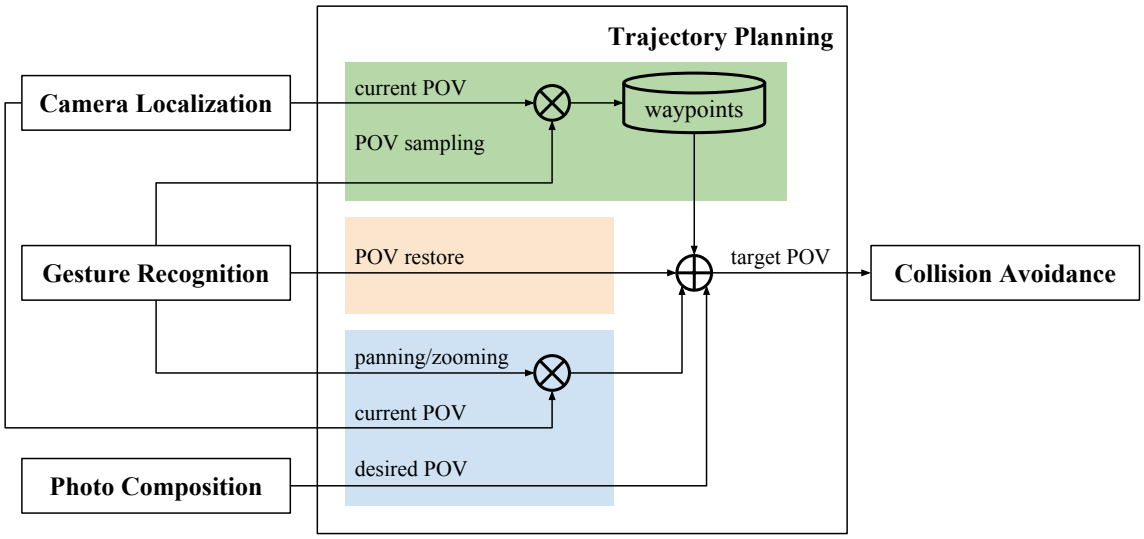

Figure 5.4: Information flow for trajectory planning component. Green block is for POV sampling. Amber block is for POV restore. Blue block is for direct view manipulation.

5.2.4 Photo Composition

Photo composition has been thoroughly studied in Chapter 3. Essentially, it translates user gestures to a user intended POV.

5.2.5 Trajectory Planning

The system generates several types of trajectories for POV sampling, POV restore, and direct view manipulation. Fig. 5.4 illustrates the information flow, in which the green block is for POV sampling, the amber block is for POV restore, and the blue block is for direct view manipulation. Next, we describe each type in detail respectively.

5.2.5.1 POV Sampling

We now describe POV sampling trajectory under each exploration mode. See Fig. 2.2.

Orbit To start the Orbit mode, XPose requires a main object of interest to be selected. The Orbit mode generates a full circular trajectory of POVs looking inward at the object. Formally speaking, the circle is essentially a line of latitude on a sphere, of which the center is the object centroid in the map, and the radius of the sphere is the distance from the object centroid to the camera position where the Orbit mode starts. For each camera position along the circle, a camera orientation is computed to maintain the object composition on the image plane.

The sample shots are planned to be taken evenly along the circle. However, since a drone can hardly reach a planned POV exactly, the sampling condition is relaxed from reaching an exact POV to entering a region of satisfied POVs. The region is bounded by various factors: the composition error, the distance difference to the object centroid, the latitude and longitude angle differences of the sphere centered at the object.

Pano The Pano mode does not require an object of interest to be selected. It generates a trajectory of POVs by spinning around at a fixed point. In other words, the POVs have the same camera position and tilt angle, but different camera pan angles.

The sample shots are taken at evenly distributed pan angles. Again, a region of satisfied POVs is used, which is bounded by the position displacement and the orientation difference.

Zigzag The trajectory generation and execution of the Zigzag mode are very similar to that of the Orbit mode. The Zigzag mode also requires a main object of interest to be selected. The major difference is the sampling pattern. Considering the sphere centered at the object, the Zigzag mode samples POVs on a patch of the sphere by deviating locally from the camera position where the Zigzag mode starts. The patch

is discretized as multiple circular arcs along different latitudes of the sphere. During execution, the drone moves along each arc one by one.

5.2.5.2 POV Restore

For POV restore, the trajectory is simply a line segment connecting the current POV and the target POV to be restored. Potential collisions are handled in the next collision avoidance component.

The end of a POV restoring trajectory is a region of POVs around the target POV, which is bounded by the position displacement and the orientation difference.

5.2.5.3 Direct View Manipulation

For direct view manipulation, the trajectory is also a line segment, but connecting from the current POV to the user desired POV according to different gestures.

The target POV for a panning/zooming gesture (Fig. 2.1) is computed based on the current POV and the corresponding intended camera motion. For example, the target POV for a zooming-in gesture is a POV in front of the current image plane along the camera's principal axis.

The target POV for direct object composition is simply the desired POV computed from the photo composition component.

5.2.6 Collision Avoidance

As illustrated in Fig. 4.2, we pursue a modular approach to collision avoidance. The collision avoidance component consists of two main parts: mapping and planning. For mapping, we aggregate individual depth maps to construct a metric-scaled occupancy grid map (Sec. 5.2.6.1). Then, we use the standard potential field algorithm to plan a collision-free path (Sec. 5.2.6.2).

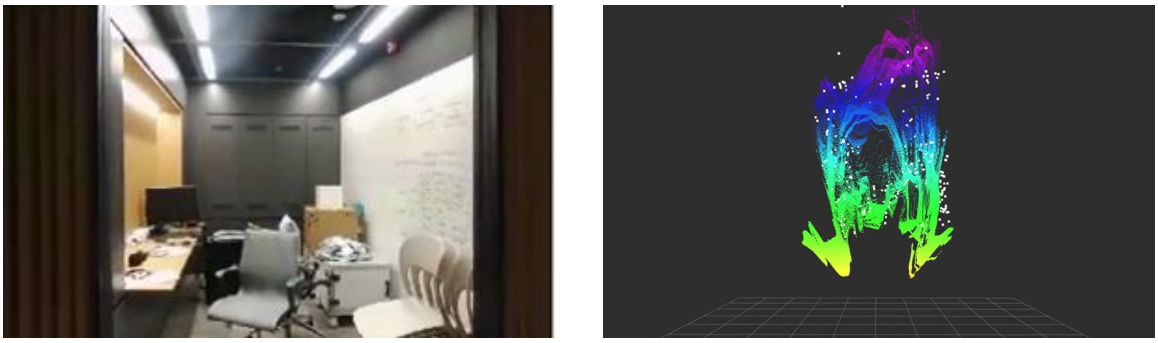

(a) (b)

Figure 5.5: Local depth map as a 3D point cloud. (a) RGB image input. (b) Our accurate dense depth map (colored point cloud) and the sparse depth map estimated by ORB-SLAM (white point cloud). The depth maps are visualized in 3D. The bottom plane corresponds to the image plane.

5.2.6.1 Occupancy Grid Mapping

There are two steps to construct a metric-scaled occupancy grid map as follows.

Depth Maps in Metric Scale First, we construct local depth maps as 3D point clouds using our pipeline proposed in Sec. 4.1. Fig. 5.5 shows an example. Fig. 5.5b is the resulting depth map visualized in 3D. Since the scale of our constructed depth map is consistent with the scale provided by ORB-SLAM. To recover the metric scale, we adopt a scale estimation method using the onboard ultrasonic altitude measurement [Engel *et al.*, 2014b].

Aggregated Occupancy Grid Map Then, we aggregate the local depth map point clouds by transforming them to the world frame using their corresponding camera poses [Hornung *et al.*, 2013].

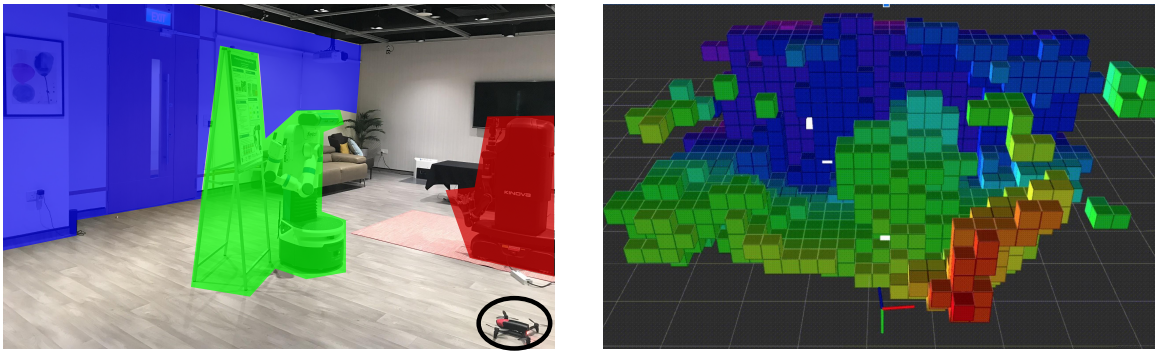

(a) (b)

Figure 5.6: Aggregated occupancy grid map. (a) The flying camera (circled in black) and the scene. Regions masked with different colors correspond to the same colored occupancy grids in (b). (b) The aggregated occupancy grid map. The RGB colored visual marker indicates the flying camera pose landed on the floor.

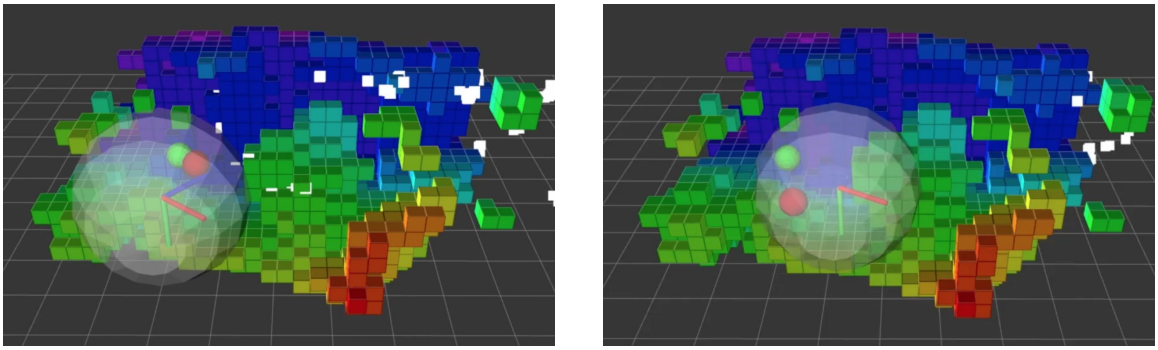

(a) (b)

Figure 5.7: Local trajectory planning. The small green sphere indicates the user target POV, i.e., the input to the collision avoidance component. The small red sphere indicates the intermediate POV, i.e., the output from the component. The big white sphere indicates the local region in which the occupancy grids are considered. (a) Very few occupancy grids are within the flying camera's local region. The intermediate POV pulls the flying camera towards the target POV. (b) The flying camera is close to obstacles that push the flying camera away.

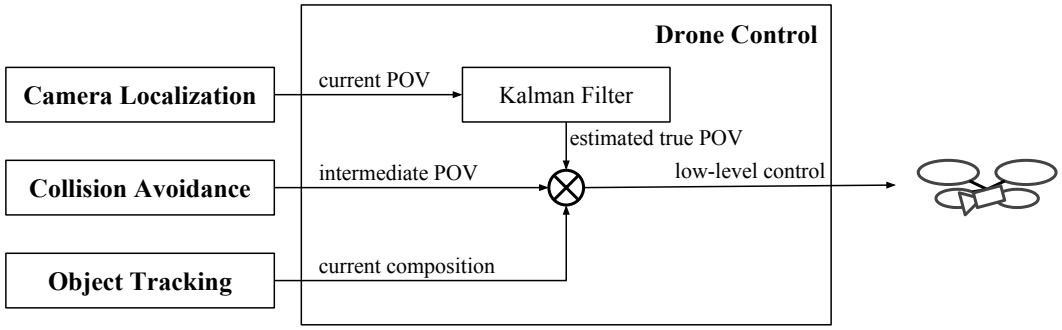

Figure 5.8: Information flow for drone control component.

5.2.6.2 Local Trajectory Planning

Next, we apply the potential field algorithm to plan for a collision-free path based on the occupancy grid map. Fig. 5.7 shows an example. We apply the potential field algorithm to generate an intermediate POV (small red sphere) based on the current camera pose and the user target POV (small green sphere) at each time step.

5.2.7 Drone Control

XPose is implemented based on the Parrot Bebop quadcopter, with a forward-facing onboard camera. The drone has a built-in digital stabilization module to fix the camera's roll. We model the state of the drone together with its onboard camera as $\mathbf{s} = [\Phi, \Theta, \dot{\Psi}, \dot{z}, \psi, \theta]^T$ with the following 6 Degrees-of-Freedom (DoFs): the drone's roll Φ and pitch Θ angles, yaw rotational velocity $\dot{\Psi}$, vertical velocity $\dot{z}$, and the camera's pan ψ and tilt θ angles. A control command $\mathbf{u} = [\bar{\Phi}, \bar{\Theta}, \bar{\dot{\Psi}}, \bar{\dot{z}}, \bar{\psi}, \bar{\theta}]^T$ sets the reference values for the onboard firmware to control the 6 DoFs respectively.

We use 6 independent PID controllers for each DoF. The control gains are tuned by assuming that the SLAM map is in the metric unit.

XPose controls the drone to reach the intermediate POV generated by the collision avoidance component. If there are any selected objects of interest, the controls of pan

and tilt angles are overwritten in order to directly minimize the composition error.

We define F^{W} as the world coordinate frame. We further denote the intermediate POV as $\hat{\mathbf{p}}^{\mathrm{W}} = [\hat{x}^{\mathrm{W}}, \hat{y}^{\mathrm{W}}, \hat{z}^{\mathrm{W}}, \hat{\psi}^{\mathrm{W}}, \hat{\theta}^{\mathrm{W}}]^T$, which consists of 3-DoF camera position $[\hat{x}^{\mathrm{W}}, \hat{y}^{\mathrm{W}}, \hat{z}^{\mathrm{W}}]^T$ and 2-DoF orientation (pan $\hat{\psi}^{\mathrm{W}}$ and tilt $\hat{\theta}^{\mathrm{W}}$).

During trajectory execution, the POV estimated by ORB-SLAM cannot be directly used, due to the delay caused by video transmission (∼200ms) and processing (∼20ms). A delayed estimation of POV may cause oscillating behaviors while controlling the system at a high update rate. To compensate the delay, a Kalman Filter is used to estimate the true POV with a constant-velocity model. This estimated POV at time t, denoted as $\mathbf{p}_t^{\mathrm{W}} = [x_t^{\mathrm{W}}, y_t^{\mathrm{W}}, z_t^{\mathrm{W}}, \psi_t^{\mathrm{W}}, \theta_t^{\mathrm{W}}]^T$, is then used to compute the low-level control commands. While our method serves the purpose of system evaluation (Chap. 6), there are more sophisticated methods [Engel *et al.*, 2014b] if needed.

Finally, the 3-DoF camera position $[\hat{x}^{\mathrm{W}}, \hat{y}^{\mathrm{W}}, \hat{z}^{\mathrm{W}}]^T$ is achieved by controlling the drone's roll Φ and pitch Θ angles, and vertical velocity $\dot{z}$. The tilt angle $\hat{\theta}^{\mathrm{W}}$ is achieved by controlling the camera's tilt θ. The pan angle $\hat{\psi}^{\mathrm{W}}$ is jointly controlled by the yaw rotational velocity $\dot{\Psi}$ and the camera's pan ψ.

Chapter 6

System Evaluation

We conducted a user study to compare XPose and a joystick interface, in order to examine the feasibility of XPose and quantify the performance differences between the two.

6.1 Experimental Setup

The study consists of two sets of experiments. The first set focuses on interaction design. It evaluates XPose's design of POV exploration and of visual composition separately. To avoid confounding factors resulting from the system implementation, it places the flying camera in a motion capture studio, which provides highly accurate camera localization and object tracking at 50 Hz. The second set of experiments focus on the overall system performance in more realistic settings, without the help of a motion capture system.

We compare XPose with one of the Parrot Bebop's native interfaces, the *Joypad* mode in the *FreeFlight Pro* app. Joypad emulates a joystick interface on a touchscreen and provides the user low-level manual control of the drone (Fig. 1.2a). We use it as the baseline for comparison, as joysticks and emulated joystick interfaces are widely

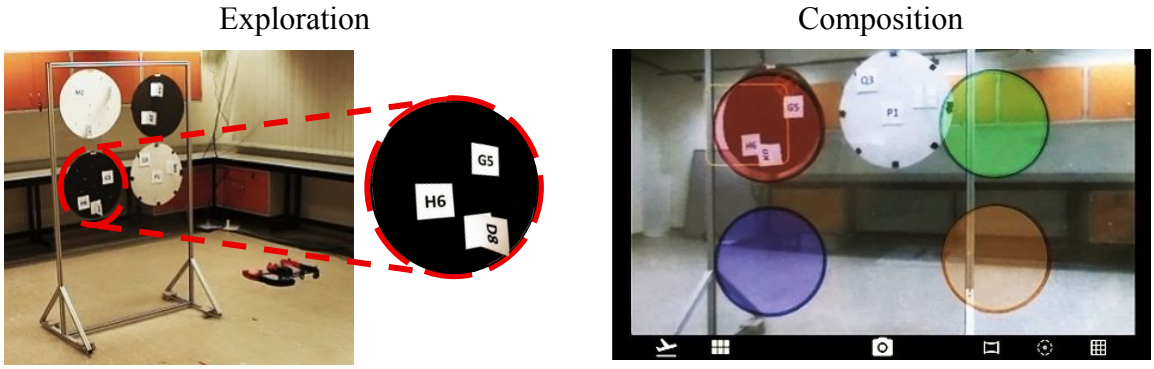

Figure 6.1: Interaction design evaluation setup. (a) Evaluation of POV exploration. Text labels are pinned at different orientations on the board. (b) Evaluation of photo composition. Four translucent colored circles indicate possible composition locations in the photo.

used in commercial drones available today. In addition, they do not depend on GPS availability, which is the intended usage scenario for XPose.

6.2 Interaction Design Evaluation

6.2.1 Evaluation of POV Exploration

The explore stage aims to find potentially interesting POVs. We designed a task to evaluate the effectiveness of POV exploration in a controlled lab setting. The setup consists of a transparent board with several target regions of interest on both sides (Fig. 6.1a). Each target region is made of a piece of circular cardboard and contains several text labels pinned at different orientations. One can see the text on the label only from a certain viewing angle range. The text on each label is unique. In each trial, the flying camera is initially placed at a fixed location on the floor 2 meters away from the board. The participant is instructed to face away from the flying camera. S/he interacts with the flying camera through the tablet only and has no direct line sight. According to our interview study, drones often fly out of the direct sight of

operators. The participant is asked to read out all the text labels on the board as fast as possible. The trial terminates when the participant believes that s/he has finished reading all the text labels and lands the flying camera. The trial pauses, if the flying camera crashes. The drone is placed on the floor at the crash site. The trial resumes after the participant relaunches the drone and continues with the task.

We measured the *completion time* for each trial and the *coverage*, *i.e.*, the percentage of correctly reported text labels.

6.2.2 Evaluation of Visual Composition

Once a potential POV is identified, the compose stage aims to place objects of interest at desired locations in the photo by refining the POV. We designed another evaluation task for composition, with a similar setup. In each trial, the participant sees in the viewfinder four circles of different colors, placed in the photo frame according to the rule of thirds (Fig. 6.1b). S/he is asked to put a specified target region at the location of a randomly assigned circle so that they match as well as possible.

Again, we measured the *completion time* for each trial as well as the *composition error* (Eq. (3.1)), which provides one measure of composition quality.

6.2.3 Experimental Design

Participants 8 volunteers (2 female, 6 male, aged 23–30) were recruited from the university community and the IT industry. All participants had prior experience taking photos, and 3 had experience flying drones.

Within-Participants Design Each participant used each interface to perform each of the two evaluation tasks three times. The order of trying the two interfaces was counterbalanced. The two tasks were ordered sequentially, as we were not interested

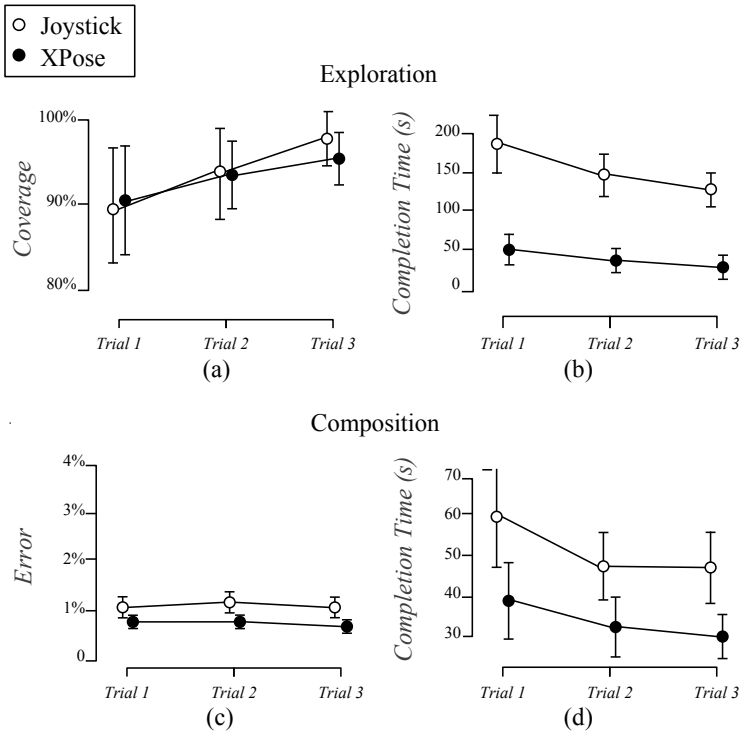

Figure 6.2: Performance comparison between the joystick interface and XPose in interaction design evaluation. Error bars indicate 95% confidence intervals.

in comparing between different tasks. Before the experiment, each participant was instructed for 10 minutes for each interface to get familiar with it.

6.2.4 Results

We conducted two-way repeated measure ANOVA to analyze the results.

POV Exploration The difference between XPose (93.1%) and the joystick interface (93.6%) in POV coverage was not significant (all $p > 0.05$). See Fig. 6.2a. The participants were able to identify most text labels (POVs) using either interfaces.

However, Fig. 6.2b shows that XPose (85.4s) was significantly faster ($F_{1,7} = 46.36,\ p < 0.001,\ \eta^2 = 0.87$) than the joystick interface (153.9s). We also observed

a significant trend ($F_{2,14} = 14.72,\ p < 0.001,\ \eta^2 = 0.68$) on completion time over the trials, indicating a learning effect for participants for both interfaces. Since most participants were not familiar with drone flying, this effect was expected. However, there was no significant interaction between the effect of interface and that of a trial on the completion time ($p > 0.05$), suggesting that the learning curves of the two interfaces are similar.

Visual Composition The composition error using XPose (0.86%) was smaller than that of the joystick interface(1.28%). See Fig. 6.2c. While the difference was statistically significant ($F_{1,7} = 21.336,\ p = 0.002,\ \eta^2 = 0.75$), both errors were about 1% and unlikely to make much difference in most photos. We did not observe any other main effects or interaction effects (all $p > 0.05$).

Again, Fig. 6.2d shows that XPose (34.2s) was significantly faster ($F_{1,7} = 24.36,\ p = 0.002,\ \eta^2 = 0.78$) than the joystick interface (47.8s). The participants also became significantly faster over trials ($F_{2,14} = 7.65,\ p = 0.006,\ \eta^2 = 0.52$), and there was no significant interaction between the effect of interface and that of trial on the completion time ($p > 0.05$).

Overall, XPose was significantly faster than the joystick interface in both POV exploration and photo composition, while achieving a comparable level of task performance measured in POV coverage or composition error. Although the number of participants in the study is relatively small, the confidence intervals are clearly separated (Fig. 6.2b,d).

6.3 System Performance Evaluation

We conducted the second set of experiments to evaluate the system performance using more realistic photo-taking settings, by removing the motion capture system. We use

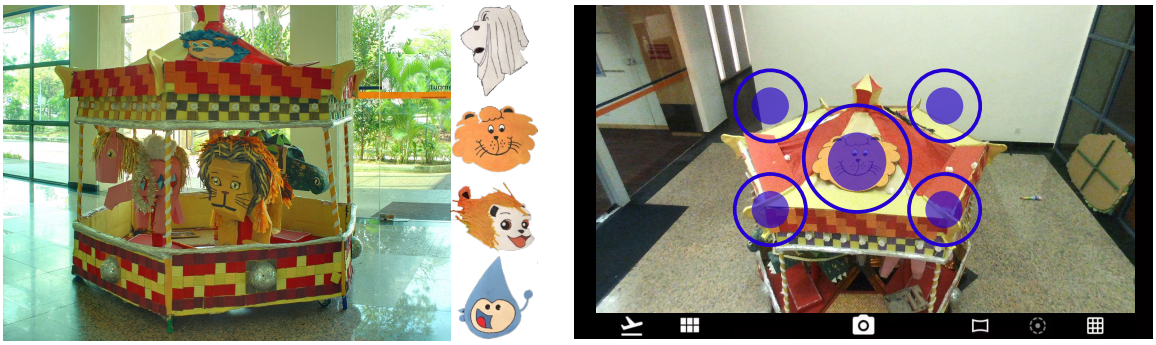

(a) (b)

Figure 6.3: System performance evaluation setup for photo-taking of one object of interest. (a) The enlarged cartoon figures are shown next to the merry-go-round in a semi-outdoor environment. (b) Each double circle indicates a possible composition location for the cartoon figure, and its size indicates the desired size of the figure in the photo.

two different setups: one mimics the scenario of searching and composing one object of interest; the other focuses on multiple objects composition.

6.3.1 Evaluation of Photo-taking - Single Object of Interest

We set up a merry-go-round in a semi-outdoor environment and hid cartoon figures inside or on top of the merry-go-round (Fig. 6.3a). The objective is to find a specified cartoon figure and compose the photo suitably. In each trial, the flying camera is initially placed at a fixed location on the floor 3 meters away from the merry-go-round. As usual, the participant has no direct line of sight of the flying camera or the merry-go-round. The participant is asked to take a photo of a specified cartoon figure and compose the photo so that the figure appears at one of the five locations marked by double circles in the viewfinder (Fig. 6.3b). Further, the figure must fully cover the inner circle and be fully enclosed by the outer circle. The trial starts after the participant launches the drone and terminates when the participant takes a shot. Each trial uses a different cartoon figure.

We measured the task *completion time* for each trial and the *success rate*.

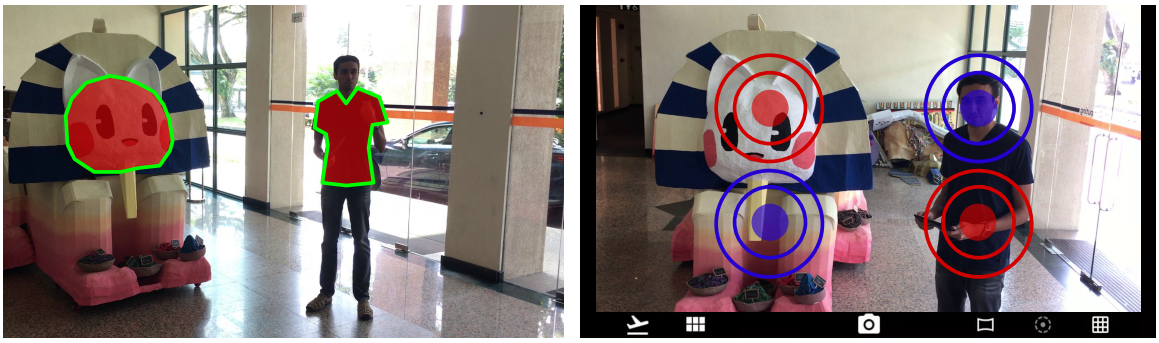

(a) (b)

Figure 6.4: System performance evaluation setup for photo taking of multiple objects of interest. (a) The highlighted cat face and the person's upper body are objects of interest. (b) Each bullseye region indicates a possible composition location for the object of interest.

6.3.2 Evaluation of Photo-taking - Multiple Objects of Interest

We set up a cat-face statue in a semi-outdoor environment (Fig. 6.4a). The objective is to take a selfie with the statue by applying the rule of thirds. In each trial, the participant stands at a fixed location near the statue. The flying camera is initially placed at a fixed location on the floor 3 meters away in front of the participant. In this setting, the participant is free to have a direct line of sight of the flying camera. The participant is asked to take a photo so that his/her upper body and the cat face appear respectively at two locations marked by the bullseye regions in the viewfinder (Fig. 6.4b).

The bullseye regions are designed to measure composition accuracy. If an object of interest (i.e., the upper body or the cat face) overlaps with its corresponding bullseye's inner circle, a score of 3 is given. Otherwise, a score of 2 is given for overlapping with the middle circle, a score of 1 is given for overlapping with the outer circle, and no score is given for non-overlapping. The composition accuracy is computed as the product of the two scores. The trial starts after the participant launches the drone and terminates when the participant takes a shot.

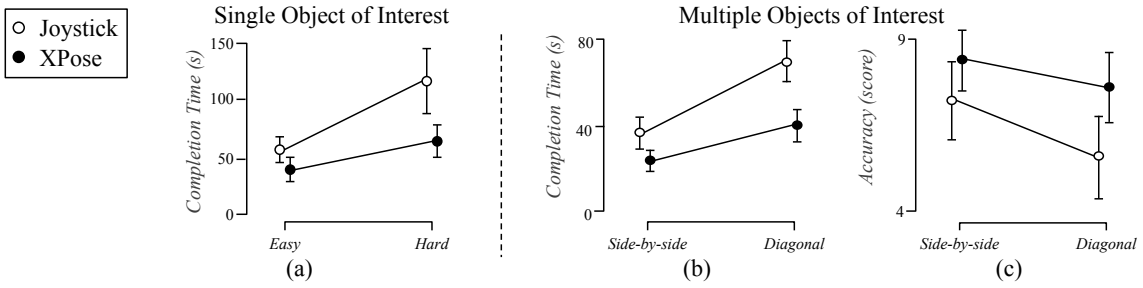

Figure 6.5: Performance comparison between the joystick interface and XPose in overall system performance evaluation. Error bars indicate 95% confidence intervals.

We measured the task *completion time* for each trial and the *composition accuracy*.

6.3.3 Experimental Design

Participants For each evaluation setup, 8 new volunteers were recruited from the university community. None participated in the earlier experiments. All participants had experience taking photos, and none of them are experienced drone pilots.

Within-Participants Design For the evaluation using a single object of interest, each participant used each interface to perform the task with two difficulty levels, one having an easy-to-find figure and one having a harder-to-find figure. The order of trying the interfaces was counterbalanced.

For the evaluation using multiple objects of interest, each participant used each interface to perform the task with two types of compositions: side-by-side composition and diagonal composition. A side-by-side composition refers to using the two top (or the two bottom) bullseye regions. A diagonal composition refers to using one top and one bottom bullseye regions. The order of trying the interfaces was counterbalanced.

6.3.4 Results

We conducted two-way repeated measure ANOVA to analyze the results.

Single Object of Interest The success rate was 100%, as all specified cartoon figures were found and composed as required. We analyzed the completion time (Fig. 6.5a). XPose (57.1s) was significantly faster ($F_{1,7} = 19.12,\ p = 0.003,\ \eta^2 = 0.73$) than the joystick interface (85.3s). The effect size value ($\eta^2 = .73$) again, suggests a high practical difference between the two interfaces. As expected, completing the easy task was significantly faster ($F_{1,7} = 52.79,\ p < 0.001,\ \eta^2 = 0.88$) than completing the hard task. Interestingly, there was significant interaction ($F_{1,7} = 6.10,\ p = 0.043,\ \eta^2 = 0.47$) between the effect of interface and that of difficulty on the completion time. Increased difficulty caused a large increase in the completion time for the joystick interface, but it caused a smaller increase for XPose. We propose the following reason. In the more difficult task, the cartoon figure was partially occluded. XPose provided a gallery preview so that participants could examine each sample shot closely and find the partially occluded figure faster.

Multiple Objects of Interest We analyzed both the completion time (Fig. 6.5b) and the composition accuracy (Fig. 6.5c). XPose was not only significantly faster ($F_{1,7} = 71.13,\ p < 0.001,\ \eta^2 = 0.91$) but also significantly more accurate ($F_{1,7} = 10.34,\ p = 0.015,\ \eta^2 = 0.60$) than the joystick interface. The effect size values ($\eta^2 = .91$ *and* 0.60) both suggest a high practical difference between the two interfaces. Interestingly, composing a side-by-side photo is both significantly faster ($F_{1,7} = 35.88,\ p < 0.001,\ \eta^2 = 0.84$) and more accurate ($F_{1,7} = 6.33,\ p = 0.04,\ \eta^2 = 0.48$) than composing a diagonal one. A potential reason is that the height of the statue is about the same as the height of a person. It is relatively easy for participants to compose side-by-side shots.

Similar to the case in composing single object of interest, there was significant interaction ($F_{1,7} = 12.22,\ p = 0.01,\ \eta^2 = 0.63$) between the effect of interface and that of composition type on the completion time. Again, increased difficulty caused a

large increase in the completion time for the joystick interface, but it caused a smaller increase for XPose. In this setup, a diagonal composition requires to fly a longer distance as compared with a side-by-side composition. XPose freed the participants from tedious control through autonomy.

6.4 Discussion

The evaluation results show that XPose outperforms the joystick interface in POV exploration, in visual composition, and in photo-taking. The joystick interface forces the user to pilot the drone manually through low-level motion commands. Doing so while searching for a good POV at the same time is difficult and tedious. Further, the communication delay between the flying camera and the touchscreen mobile device often causes the camera to overshoot the desired pose. Our explore-and-compose approach demonstrates great potentials for photo-taking with flying cameras. While our experiments tested only a small range of representative tasks, we are pleased to see that our interaction design enabled more efficient POV exploration with predefined exploration modes and easier photo composition with direct manipulation of objects of interest. POV exploration and photo composition are essential sub-tasks for photo taking. Creating more efficient and user-friendly approaches to these tasks contribute significantly to better photo taking. Participants expressed that XPose is more natural and intuitive to use: *"Yours (XPose) is easier to use as I can focus on the task instead of flying the drone."* More encouragingly, the two stages, explore and compose, worked well together for more realistic photo-taking tasks in a GPS-denied semi-outdoor environment. Together, the results of our user study suggest that XPose clearly represents a step forward towards a practically useful system.

Chapter 7

Conclusion

We presented XPose, a touch-based interactive system for flying camera photo-taking. XPose introduces the explore-and-compose paradigm to photo-taking and provides a unified interaction model for flying cameras. It enables a low-cost quadcopter to fly in a GPS-denied environment and provides intuitive and effective interactions that aid the user for photo-taking in real time. As a result, the user focuses on taking photos, instead of piloting the drone.

Our experience highlights the importance of integrating interaction design (Chap. 2) and system implementation (Chap. 5). Good interaction design must be rooted in realistic assumptions of system capabilities, and new system implementation technologies open up opportunities for innovative interaction design.

From the interaction design perspective, the explore-and-compose paradigm currently focuses on photo-taking in static scenes. We believe that the underlying design idea is useful for dynamic scenes as well, but the interaction design and the system implementation become more challenging. In addition, the explore-and-compose paradigm could also be adopted in other modalities, such as mouse-based interfaces.

From the system implementation perspective, our current prototype works suc-

cessfully in indoor, semi-outdoor, and limited outdoor settings, with two main limitations. First, we rely on a laptop computer for most of the required computation, because the Parrot Bebop drone has a very limited onboard processing power. Second, due to the limited viewing angle of the forward-facing camera on the Parrot Bebop, the collision-free path planning cannot be seamlessly integrated. With rapid advances in hardware technology and decreasing cost, we expect to overcome these limitations in the near future.

While our prototype implementation still has several limitations, it is a first step towards the ultimate vision of a flying camera for everyday use.

Bibliography

[AirSelfie, 2018] AirSelfie. The only portable flying camera integrated in your photo cover. `http://www.airselfiecamera.com/`, 2018.

[AutonomyLab, 2018] AutonomyLab. Bebop autonomy. `https://github.com/autonomylab/bebop_autonomy`, 2018.

[Ballou, 2001] P Ballou. Improving pilot dexterity with a telepresent rov. In *Proc. the Vehicle Teleoperation Interfaces Workshop, ICRA*, 2001.

[Bansal and Daniilidis, 2014] Mayank Bansal and Kostas Daniilidis. Geometric urban geo-localization. In *CVPR*, 2014.

[Bebop, 2018] Bebop. Parrot bebop drone. `http://global.parrot.com/au/products/bebop-drone`, 2018.

[Bloesch *et al.*, 2018] Michael Bloesch, Jan Czarnowski, Ronald Clark, Stefan Leutenegger, and Andrew J Davison. Codeslamlearning a compact, optimisable representation for dense visual slam. In *CVPR*, 2018.

[Booij *et al.*, 2009] Olaf Booij, Zoran Zivkovic, et al. The planar two point algorithm. *IAS technical report, University of Amsterdam*, 2009.

[Bowman *et al.*, 1997] Doug A Bowman, David Koller, and Larry F Hodges. Travel in immersive virtual environments: An evaluation of viewpoint motion control techniques. In *Virtual Reality Annual International Symposium*, 1997.

[Burtnyk *et al.*, 2002] Nicholas Burtnyk, Azam Khan, George Fitzmaurice, Ravin Balakrishnan, and Gordon Kurtenbach. StyleCam: interactive stylized 3D navigation using integrated spatial & temporal controls. In *UIST*, 2002.

[Byrod *et al.*, 2008] Martin Byrod, Zuzana Kukelova, Klas Josephson, Tomas Pajdla, and Kalle Astrom. Fast and robust numerical solutions to minimal problems for cameras with radial distortion. In *CVPR*, 2008.

[Camposeco *et al.*, 2017] Federico Camposeco, Torsten Sattler, Andrea Cohen, Andreas Geiger, and Marc Pollefeys. Toroidal constraints for two-point localization under high outlier ratios. In *CVPR*, 2017.

[Caruso *et al.*, 2015] David Caruso, Jakob Engel, and Daniel Cremers. Large-scale direct slam for omnidirectional cameras. In *IROS*, 2015.

[Cheerson, 2018] Cheerson. Experience the flying dream. `http://www.cheersonhobby.com/en-US/`, 2018.

[Choi and Park, 2015] Sung-In Choi and Soon-Yong Park. A new 2-point absolute pose estimation algorithm under planar motion. *Advanced Robotics*, 2015.

[Concha and Civera, 2015] Alejo Concha and Javier Civera. DPPTAM: Dense piecewise planar tracking and mapping from a monocular sequence. In *IROS*, 2015.

[DJI, 2018a] DJI. DJI Drones. `http://www.dji.com/products/drones`, 2018.

[DJI, 2018b] DJI. Inspire 1 pro-dual remote controllers mode. `http://wiki.dji.com/en/index.php/Inspire_1_Pro-Dual_Remote_Controllers_Mode`, 2018.

[Dragicevic *et al.*, 2008] Pierre Dragicevic, Gonzalo Ramos, Jacobo Bibliowitcz, Derek Nowrouzezahrai, Ravin Balakrishnan, and Karan Singh. Video browsing by direct manipulation. In *ACM SIGCHI*, 2008.

[Dronestagram, 2017] Dronestagram. International drone photography contest. `http://www.dronestagr.am/2017-international-drone-photography-contest`, 2017.

[Eigen and Fergus, 2015] David Eigen and Rob Fergus. Predicting depth, surface normals and semantic labels with a common multi-scale convolutional architecture. In *ICCV*, 2015.

[Eigen *et al.*, 2014] David Eigen, Christian Puhrsch, and Rob Fergus. Depth map prediction from a single image using a multi-scale deep network. In *NIPS*, 2014.

[Elmqvist *et al.*, 2008] Niklas Elmqvist, Mihail Eduard Tudoreanu, and Philippas Tsigas. Evaluating motion constraints for 3d wayfinding in immersive and desktop virtual environments. In *ACM SIGCHI*, 2008.

[Engel *et al.*, 2014a] Jakob Engel, Thomas Schöps, and Daniel Cremers. LSD-SLAM: Large-scale direct monocular slam. In *ECCV*, 2014.

[Engel *et al.*, 2014b] Jakob Engel, Jürgen Sturm, and Daniel Cremers. Scale-aware navigation of a low-cost quadrocopter with a monocular camera. *RAS*, 2014.

[Flynixie, 2018] Flynixie. The first wearable camera that can fly — flynixie. `http://flynixie.com`, 2018.

[Forster *et al.*, 2014] Christian Forster, Matia Pizzoli, and Davide Scaramuzza. Svo: Fast semi-direct monocular visual odometry. In *ICRA*, 2014.

[Forster *et al.*, 2017] Christian Forster, Zichao Zhang, Michael Gassner, Manuel Werlberger, and Davide Scaramuzza. Svo: Semidirect visual odometry for monocular and multicamera systems. *IEEE Transactions on Robotics*, 2017.

[Fuentes-Pacheco *et al.*, 2012] Jorge Fuentes-Pacheco, José Ruíz Ascencio, and Juan M. Rendón-Mancha. Visual simultaneous localization and mapping: a survey. *Artificial Intelligence Review*, 2012.

[Furukawa *et al.*, 2010] Yasutaka Furukawa, Brian Curless, Steven M Seitz, and Richard Szeliski. Towards internet-scale multi-view stereo. In *CVPR*, 2010.

[Galyean, 1995] Tinsley A Galyean. Guided navigation of virtual environments. In *I3D*, 1995.

[Gao *et al.*, 2003] Xiao-Shan Gao, Xiao-Rong Hou, Jianliang Tang, and Hang-Fei Cheng. Complete solution classification for the perspective-three-point problem. *TPAMI*, 2003.

[Gebhardt *et al.*, 2016] Christoph Gebhardt, Benjamin Hepp, Tobias Nägeli, Stefan Stevšić, and Otmar Hilliges. Airways: Optimization-based planning of quadrotor trajectories according to high-level user goals. In *ACM SIGCHI*, 2016.

[Geiger *et al.*, 2013] Andreas Geiger, Philip Lenz, Christoph Stiller, and Raquel Urtasun. Vision meets robotics: The kitti dataset. *IJRR*, 2013.

[Gernsheim and Gernsheim, 1969] Helmut Gernsheim and Alison Gernsheim. *The history of photography: from the camera obscura to the beginning of the modern era*. New York: McGraw-Hill, 1969.

[Gleicher and Witkin, 1992] Michael Gleicher and Andrew Witkin. Through-the-lens camera control. In *ACM SIGGRAPH*, 1992.

[Godard *et al.*, 2017] Clément Godard, Oisin Mac Aodha, and Gabriel J Brostow. Unsupervised monocular depth estimation with left-right consistency. In *CVPR*, 2017.

[Hachet *et al.*, 2008] Martin Hachet, Fabrice Decle, Sebastian Knodel, and Pascal Guitton. Navidget for easy 3D camera positioning from 2D inputs. *3DUI*, 2008.

[Hainsworth, 2001] David W Hainsworth. Teleoperation user interfaces for mining robotics. *Autonomous Robots*, 2001.

[Hanson and Wernert, 1997] Andrew J Hanson and Eric A Wernert. Constrained 3D navigation with 2D controllers. In *Visualization*, 1997.

[Hornung *et al.*, 2013] Armin Hornung, Kai M Wurm, Maren Bennewitz, Cyrill Stachniss, and Wolfram Burgard. Octomap: An efficient probabilistic 3d mapping framework based on octrees. *Autonomous robots*, 2013.

[Joubert *et al.*, 2015] Niels Joubert, Mike Roberts, Anh Truong, Floraine Berthouzoz, and Pat Hanrahan. An interactive tool for designing quadrotor camera shots. *ACM TOG*, 2015.

[Kalal *et al.*, 2012] Zdenek Kalal, Krystian Mikolajczyk, Jiri Matas, et al. Tracking-learning-detection. *TPAMI*, 2012.

[Karaman and Frazzoli, 2010] Sertac Karaman and Emilio Frazzoli. Incremental sampling-based algorithms for optimal motion planning. *RSS*, 2010.

[Karrer *et al.*, 2008] Thorsten Karrer, Malte Weiss, Eric Lee, and Jan Borchers. Dragon: a direct manipulation interface for frame-accurate in-scene video navigation. In *ACM SIGCHI*, 2008.

[Karsch *et al.*, 2014] Kevin Karsch, Ce Liu, and Sing Bing Kang. Depth transfer: Depth extraction from video using non-parametric sampling. *TPAMI*, 2014.

[Khan *et al.*, 2005] Azam Khan, Ben Komalo, Jos Stam, George Fitzmaurice, and Gordon Kurtenbach. Hovercam: interactive 3d navigation for proximal object inspection. In *I3D*, 2005.

[Khatib, 1985] Oussama Khatib. Real-time obstacle avoidance for manipulators and mobile robots. In *ICRA*, 1985.

[Klein and Murray, 2007] Georg Klein and David Murray. Parallel tracking and mapping for small ar workspaces. In *ISMAR*, 2007.

[Kukelova and Pajdla, 2007a] Zuzana Kukelova and Tomas Pajdla. A minimal solution to the autocalibration of radial distortion. In *CVPR*, 2007.

[Kukelova and Pajdla, 2007b] Zuzana Kukelova and Tomas Pajdla. Two minimal problems for cameras with radial distortion. In *ICCV*, 2007.

[Kyung *et al.*, 1996] Min-Ho Kyung, Myung-Soo Kim, and Sung Je Hong. A new approach to through-the-lens camera control. *GMIP*, 1996.

[Laina *et al.*, 2016] Iro Laina, Christian Rupprecht, Vasileios Belagiannis, Federico Tombari, and Nassir Navab. Deeper depth prediction with fully convolutional residual networks. In *3D Vision*, 2016.

[Lepetit *et al.*, 2009] Vincent Lepetit, Francesc Moreno-Noguer, and Pascal Fua. EPnP: an accurate $O(n)$ solution to the PnP problem. *IJCV*, 2009.

[Li and Snavely, 2018] Zhengqi Li and Noah Snavely. Megadepth: Learning single-view depth prediction from internet photos. In *CVPR*, 2018.

[Li *et al.*, 2012] Shiqi Li, Chi Xu, and Ming Xie. A robust O(n) solution to the perspective-n-point problem. *TPAMI*, 2012.

[Li *et al.*, 2015] Bo Li, Chunhua Shen, Yuchao Dai, Anton Van Den Hengel, and Mingyi He. Depth and surface normal estimation from monocular images using regression on deep features and hierarchical crfs. In *CVPR*, 2015.

[Lily-Next-Gen, 2017] Lily-Next-Gen. Flying robots get your lily robot. `http://www.lily.camera/`, 2017.

[Lino and Christie, 2015] Christophe Lino and Marc Christie. Intuitive and efficient camera control with the toric space. *ACM TOG*, 2015.

[Liu *et al.*, 2014] Miaomiao Liu, Mathieu Salzmann, and Xuming He. Discrete-continuous depth estimation from a single image. In *CVPR*, 2014.

[Liu *et al.*, 2015] Fayao Liu, Chunhua Shen, and Guosheng Lin. Deep convolutional neural fields for depth estimation from a single image. In *CVPR*, 2015.

[Liu *et al.*, 2016] Fayao Liu, Chunhua Shen, Guosheng Lin, and Ian Reid. Learning depth from single monocular images using deep convolutional neural fields. *TPAMI*, 2016.

[Mackinlay *et al.*, 1990] Jock D Mackinlay, Stuart K Card, and George G Robertson. Rapid controlled movement through a virtual 3d workspace. In *ACM SIGGRAPH*, 1990.

[Marder-Eppstein, 2016] Eitan Marder-Eppstein. Project tango. In *ACM SIGGRAPH Real-Time Live!*, 2016.

[McGovern, 1991] Douglas E McGovern. Experience and results in teleoperation of land vehicles. In *Pictorial Communication in Virtual and Real Environments*, 1991.

[Mei *et al.*, 2010] Christopher Mei, Gabe Sibley, and Paul Newman. Closing loops without places. In *IROS*, 2010.

[Merckel and Nishida, 2008] Loic Merckel and Toyoaki Nishida. Evaluation of a method to solve the perspective-two-point problem using a three-axis orientation sensor. In *CIT*, 2008.

[Mur-Artal *et al.*, 2015] Raul Mur-Artal, Jose Maria Martinez Montiel, and Juan D Tardos. ORB-SLAM: a versatile and accurate monocular slam system. *T-RO*, 2015.

[Nebehay and Pflugfelder, 2015] Georg Nebehay and Roman Pflugfelder. Clustering of static-adaptive correspondences for deformable object tracking. In *CVPR*, 2015.

[Newcombe *et al.*, 2011] Richard A Newcombe, Steven J Lovegrove, and Andrew J Davison. Dtam: Dense tracking and mapping in real-time. In *ICCV*, 2011.

[Nicholas Greene and Roy, 2017] W Nicholas Greene and Nicholas Roy. FLaME: Fast Lightweight Mesh Estimation Using Variational Smoothing on Delaunay Graphs. In *ICCV*, 2017.

[Nistér, 2004] David Nistér. An efficient solution to the five-point relative pose problem. *TPAMI*, 2004.

[Pizzoli *et al.*, 2014] Matia Pizzoli, Christian Forster, and Davide Scaramuzza. REMODE: Probabilistic, monocular dense reconstruction in real time. In *ICRA*, 2014.

[Reisman *et al.*, 2009] Jason L Reisman, Philip L Davidson, and Jefferson Y Han. A screen-space formulation for 2d and 3d direct manipulation. In *UIST*, 2009.

[Rockafellar and Wets, 2009] R Tyrrell Rockafellar and Roger J-B Wets. *Variational analysis*, volume 317. Springer Science & Business Media, 2009.

[Ross *et al.*, 2013] Stéphane Ross, Narek Melik-Barkhudarov, Kumar Shaurya Shankar, Andreas Wendel, Debadeepta Dey, J Andrew Bagnell, and Martial Hebert. Learning monocular reactive uav control in cluttered natural environments. In *ICRA*, 2013.

[Sadeghi and Levine, 2017] Fereshteh Sadeghi and Sergey Levine. $(\text{CAD})^2\text{RL}$: Real single-image flight without a single real image. In *RSS*, 2017.

[Satou *et al.*, 1999] Takashi Satou, Haruhiko Kojima, Akihito Akutsu, and Yoshinobu Tonomura. Cybercoaster: Polygonal line shaped slider interface to spatio-temporal media. In *ACM Multimedia*, 1999.

[Saxena *et al.*, 2009] Ashutosh Saxena, Min Sun, and Andrew Y Ng. Make3d: Learning 3d scene structure from a single still image. *TPAMI*, 2009.

[Schonberger and Frahm, 2016] Johannes L Schonberger and Jan-Michael Frahm. Structure-from-motion revisited. In *CVPR*, 2016.

[Schöps *et al.*, 2017] Thomas Schöps, Johannes L. Schönberger, Silvano Galliani, Torsten Sattler, Konrad Schindler, Marc Pollefeys, and Andreas Geiger. A multi-view stereo benchmark with high-resolution images and multi-camera videos. In *CVPR*, 2017.

[Siek *et al.*, 2005] Katie A Siek, Yvonne Rogers, and Kay H Connelly. Fat finger worries: how older and younger users physically interact with PDAs. In *INTERACT*, 2005.

[Silberman and Fergus, 2011] Nathan Silberman and Rob Fergus. Indoor scene segmentation using a structured light sensor. In *Computer Vision Workshops (ICCV Workshops)*, 2011.

[Skydio-R1, 2018] Skydio-R1. Skydio the self-flying camera has arrived. `https://www.skydio.com/`, 2018.

[Stewénius *et al.*, 2008] Henrik Stewénius, David Nistér, Fredrik Kahl, and Frederik Schaffalitzky. A minimal solution for relative pose with unknown focal length. *Image and Vision Computing*, 2008.

[Strasdat *et al.*, 2011] Hauke Strasdat, Andrew J Davison, JM Martìnez Montiel, and Kurt Konolige. Double window optimisation for constant time visual slam. In *ICCV*, 2011.

[Tang and Tan, 2018] Chengzhou Tang and Ping Tan. Ba-net: Dense bundle adjustment network. *arXiv preprint arXiv:1806.04807*, 2018.

[Triggs, 1999] Bill Triggs. Camera pose and calibration from 4 or 5 known 3d points. In *ICCV*, 1999.

[Umeyama, 1991] Shinji Umeyama. Least-squares estimation of transformation parameters between two point patterns. *TPAMI*, 1991.

[Urban *et al.*, 2016] Steffen Urban, Jens Leitloff, and Stefan Hinz. MLPnP-a real-time maximum likelihood solution to the perspective-n-point Problem. *ISPRS journal of photogrammetry and remote sensing*, 2016.

[Walther-Franks *et al.*, 2011] Benjamin Walther-Franks, Marc Herrlich, and Rainer Malaka. A multi-touch system for 3D modelling and animation. In *International Symposium on Smart Graphics*, 2011.

[Ware and Osborne, 1990] Colin Ware and Steven Osborne. Exploration and virtual camera control in virtual three dimensional environments. *ACM SIGGRAPH*, 1990.

[Xu *et al.*, 2017] Dan Xu, Elisa Ricci, Wanli Ouyang, Xiaogang Wang, and Nicu Sebe. Multi-scale continuous crfs as sequential deep networks for monocular depth estimation. In *CVPR*, 2017.

[Zeleznik and Forsberg, 1999] Robert Zeleznik and Andrew Forsberg. UniCam2D gestural camera controls for 3D environments. In *I3D*, 1999.

[Zheng *et al.*, 2013] Yinqiang Zheng, Yubin Kuang, Shigeki Sugimoto, Kalle Astrom, and Masatoshi Okutomi. Revisiting the pnp problem: a fast, general and optimal solution. In *ICCV*, 2013.

[Zhou *et al.*, 2017] Tinghui Zhou, Matthew Brown, Noah Snavely, and David G Lowe. Unsupervised learning of depth and ego-motion from video. In *CVPR*, 2017.